ARISTOTLE UNIVERSITY OF THESSALONIKI
DEPARTMENT OF ELECTRICAL AND
COMPUTER ENGINEERING

Improved CERN LHC layout and aperture models

Lampaki Syrmatenia

Diploma Thesis

Supervisor: Dr. Riccardo De Maria, CERN

Supervisor: Dr. Nikolaos Kantartzis, AUTh

Thessaloniki, June 2024

ΑΡΙΣΤΟΤΕΛΕΙΟ ΠΑΝΕΠΙΣΤΗΜΙΟ ΘΕΣΣΑΛΟΝΙΚΗΣ
ΤΜΗΜΑ ΗΛΕΚΤΡΟΛΟΓΩΝ ΜΗΧΑΝΙΚΩΝ
ΚΑΙ ΜΗΧΑΝΙΚΩΝ ΥΠΟΛΟΓΙΣΤΩΝ

Βελτιωμένα μοντέλα διάταξης και διαφραγμάτων στον Μεγάλο Επιταχυντή Αδρονίων του CERN

Λαμπάκη Συρματένια

Διπλωματική Εργασία

Επιβλέπων: Dr. Riccardo De Maria, CERN

Επιβλέπων: Δρ. Νικόλαος Κανταρτζής, ΑΠΘ

Θεσσαλονίκη, Ιούνιος 2024

Acknowledgments

I would like to thank my supervisor at CERN, Dr. Riccardo De Maria, firstly, for giving me the opportunity to work on this project. Thank you for sharing your incredible knowledge, skills and passion in accelerator physics, and of course, for answering my questions, despite your extremely busy schedule.

I would therefore like to thank my supervisor at the Aristotle University of Thessaloniki, Dr. Nikolaos Kantartzis, for his trust and support all along.

Last, I want to thank Joao Oliveira, Bruno Feral, Frederik Van Der Veken and Bjorn Lindstrom for their valuable help, feedback, and inputs in times needed.

Abstract

Aperture models are of fundamental importance to design machine optics configurations and predict machine performance. They are also essential to detect design flaws during the engineering and construction phase, and essential to steer alignment campaigns and optimize operational scenarios.

The project consists in developing automatic tools to create beam aperture models from the CERN layout database and survey measurements in MAD-X format. Combined with beam optics models, this allows performing consistency checks and improve data quality, as well as obtaining detailed aperture analysis for the LHC that will serve as a basis to optimize the machine operational scenarios and performance.

Keywords: CERN, LHC, Beam Dynamics, Accelerator Physics, aperture, layout, LDB, MAD-X, PyLayout, TDIS, TCLIA, Superconducting RF Cavities

Περίληψη

Τα μοντέλα διαφράγματος είναι θεμελιώδους σημασίας για τον σχεδιασμό των διατάξεων οπτικής των επιταχυντών και την πρόβλεψη της απόδοσής τους. Είναι επίσης απαραίτητα για τον εντοπισμό των σχεδιαστικών ατελειών κατά τη φάση της σχεδιαστική μελέτης και της κατασκευής, καθώς και για την καθοδήγηση των διαδικασιών ευθυγράμμισης και τη βελτιστοποίηση των λειτουργικών σεναρίων.

Το εν λόγω έργο συνίσταται στην ανάπτυξη αυτόματων εργαλείων για τη δημιουργία μοντέλων διαφράγματος δέσμης από τη βάση δεδομένων της διάταξης των επιταχυντών του CERN (Layout DB) και από τοπογραφικές μετρήσεις, σε μορφή MAD-X. Σε συνδυασμό με τα μοντέλα δέσμης οπτικής (beam optics model), αυτό επιτρέπει τη διενέργεια ελέγχων συνέπειας και συνοχής, τη βελτίωση της ποιότητας των δεδομένων, καθώς και την απόκτηση λεπτομερούς ανάλυσης του διαφράγματος για τον Μεγάλο Επιταχυντή Αδρονίων (LHC), η οποία θα χρησιμεύσει ως βάση για τη βελτιστοποίηση των λειτουργικών σεναρίων και των επιδόσεών του .

Λέξεις κλειδιά: CERN, Μεγάλος Επιταχυντής Αδρονίων, Δυναμική Δεσμών, Φυσική Επιταχυντών, διαφράγματα, διάταξη, LDB, MAD-X, PyLayout, TDIS, TCLIA, Superconducting RF Cavities

Contents

List of Figures

List of Tables

Chapter 1
Introduction

1.1 Introduction to accelerator physics

In accelerator physics, the dynamics of charged particles are governed mainly by the classical effect of electromagnetism and, in higher energies, under a relativistic regime. Quantum effects are involved during collisions and in the presence of strong synchrotron radiation, therefore they will not be considered in this study.

A charged particle that travels through an electromagnetic field feels the Lorentz force:

$$\vec{F} = \frac{d\vec{p}}{dt} = q(\vec{v} \times \vec{B} + \vec{E}). \tag{1.1}$$

In the presence of a magnetic field $\vec{B}$, the force acts perpendicular to the path of the particle, thus it can change the direction of it (deflect it). In contrast, when the particle is subjected to an electric field $\vec{E}$, the force acts parallel to the path of the particle, and it can accelerate it, but $\vec{E}$ is not optimal for deflection.

Typically, in synchrotrons (like the LHC), dipole magnets generate a uniform transverse magnetic field that guides the beam around a circular orbit, and a set of Radio Frequency (RF) cavities provides acceleration and stability for the longitudinal motion. Then the quadrupole magnets provide transverse stability and, lastly, other multipole corrector magnets (sextupoles, octupoles, etc.) provide additional stability by correcting natural aberrations and imperfections.

A typical simplified synchrotron accelerator has the layout depicted in Figure 1.1. Considering only linear magnets (dipoles: blue, quadrupoles: orange), the gray circular line is the beam pipes, hosting the two counterotating beams, under high vacuum. The beam, coming from a previous accelerator, enters the accelerator through an injection mechanism. The beams are accelerated in each turn in the small acceleration gap by the RF cavities. Finally, the beam leaving the accelerator might go to another accelerator, to a target (a physics experiment) or it will be dumped since its quality has been degraded.

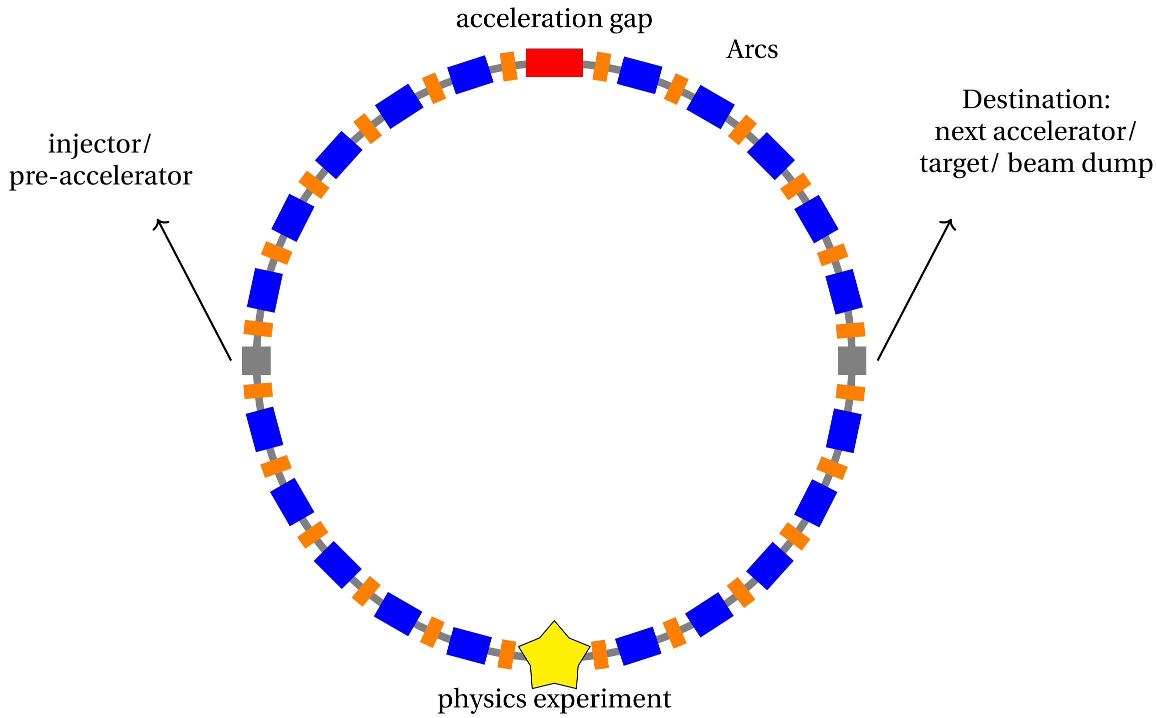

Figure 1.1: A typical simplified synchrotron.

1.1.1 Coordinate Systems

At this point, it is useful to define the coordinate systems that we will be referring to.

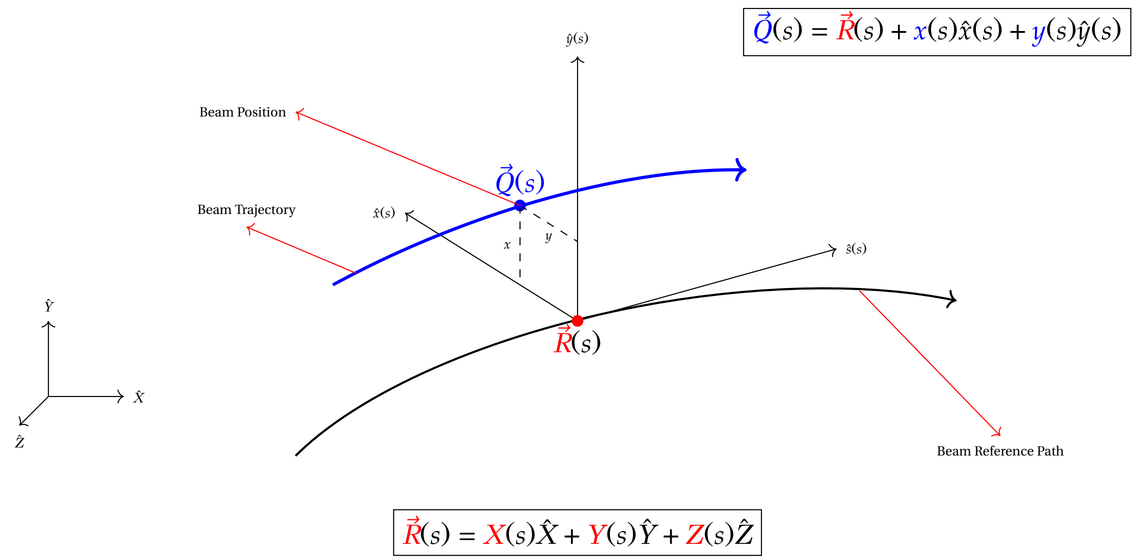

Figure 1.2: Beam trajectories as deviations from the reference path

Beam (or single particle) trajectories are calculated as deviations from a continuous reference path. A point on the reference path is identified by the accumulated path length (s or DCUM, cumulative distance) from the start of the path.

Using MAD-X as reference: $\vec{S}$ is the direction of the beam, $\vec{Y}$ is the vertical direction, $\vec{X}$ points to a horizontal direction orthogonal to $\vec{S}$ and $\vec{Y}$. In MAD-X, a positive bending angle corresponds to a trajectory turning clock-wise when seen from the top. The positive $\vec{X}$ direction points to the outside of the trajectory. Layout DB presents position information in the main window as S, U, and V. Internal tables and some accessory GUI with the same coordinates are labeled X, Y, and Z.

MAD-X	x	y	s
Layout DB Web UI	-U	V	S
Layout DB internal	-Y	Z	X
Mechanical drawings	-X	Z	Y
Fiducialization	-R	T	S

Table 1.1: Comparison between axis names of the local reference systems.

LHC and multiple beams

Beam 1 and Beam 2 have different reference paths. The LHC layout in the LDB (is defined using the mid-beam using a “straight” coordinate system SUV (see Figure 1.3).

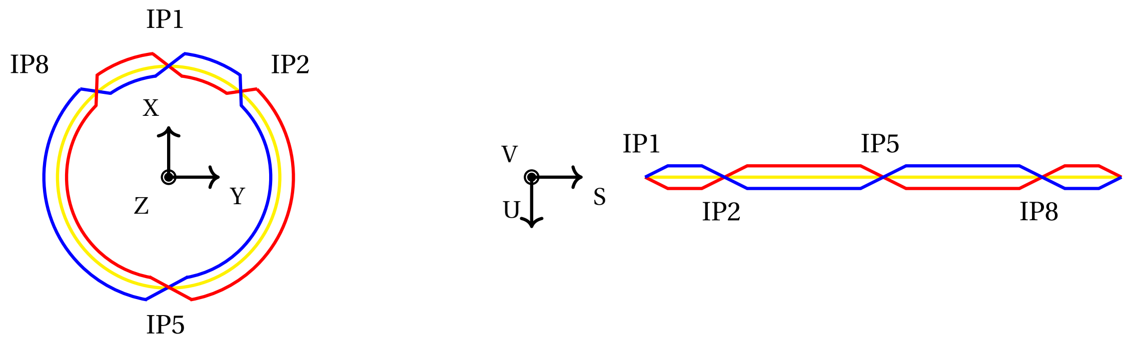

Figure 1.3: Illustrative, not in scale, representation of the Beam 1 (blue), Beam 2 (red), and mid-beam (yellow) reference paths in the LHC in CCS coordinates (left) and SUV coordinates (right). The S coordinates are used to indicate the DCUM of the mid-beam and the UV of the transverse position.

1.1.2 Transverse beam Dynamics

The ideal circular orbit

The ideal circular orbit can be deduced if one considers the Lorentz Force ($F_L = qvB$) and centrifugal Force ($F_{\text{centr}} = \frac{\gamma m_0 v^2}{\rho}$), thus:

$$F_L = F_{\text{centr}} \Rightarrow \frac{p}{q} = B\rho = \text{Beam rigidity}, \tag{1.2}$$

where q is the charge, B the magnetic field strength, $p = \gamma m_0 v$ the momentum and ρ bending radius. The Beam rigidity tells us how strongly we have to pull on the particles with a given magnetic field in order to keep them on the defined radius, depending on their energy, momentum, and charge.

Then, the required magnetic field strength will be:

$$B = \frac{2\pi p}{qNl}. \tag{1.3}$$

The design orbit, which is the trajectory of the ideal particle, is defined by dipole magnets. But, in a homogeneous magnetic field, particles with varying initial conditions fulfill oscillations around the design orbit, and this will lead to Betatron oscillation. Evidently, a bunch contains many particles with different initial conditions, leading to many different positions, angles, and energy offsets. Therefore, we need a focusing force that keeps the particles close to the design orbit. This force should rise as a function of the distance to the design orbit. The requirement is that the Lorentz force should be linearly increasing as a function of distance from the design orbit. Thus, a linearly increasing magnetic field.

$$F(x) = qvB(x). \tag{1.4}$$

Taylor series as function of distance from magnet center

$$B_y(x) = B_{y0} + \frac{\partial B_y}{\partial x}x + \frac{1}{2}\frac{\partial^2 B_y}{\partial x^2}x^2 + \frac{1}{3!}\frac{\partial^3 B_y}{\partial x^3}x^3 + \cdots \tag{1.5}$$

dipole quadrupole sextupole octupole higher orders

Normalized to p/q:

$$\frac{B_y(x)}{p/q} = \frac{1}{\rho} + \boxed{kx} + \frac{1}{2}mx^2 + \frac{1}{3!}nx^3 + \cdots \tag{1.6}$$

quadrupole

Hence, we can focus the particles with quadrupoles, with the vertical (y) and horizontal (x) quadrupole fields:

$$B_y = g \cdot x, \quad B_x = g \cdot y, \tag{1.7}$$

where g is the gradient

$$g = \frac{2\mu_0 nI}{r^2}\left[\frac{T}{m}\right], \tag{1.8}$$

and the normalized gradient defines the focusing strength

$$k = \frac{g}{p/q}\left[m^{-2}\right], \tag{1.9}$$

where I: coil current, n: number of windings, r: distance between the magnet center and the pole, μ_0: permeability of free space.

Quadrupoles focus on one plane, and defocus on the other! But, focusing particles with quadrupoles is similar to focusing light with lenses. A series of alternating focusing and defocusing lenses will focus:

$$\frac{1}{F} = \frac{1}{f_1} + \frac{1}{f_2} - \frac{d}{f_1 f_2}. \tag{1.10}$$

Considering: $f_1 = f, f_2 = -f$, Then: $F = \frac{f^2}{d} > 0$.

In a synchrotron, quadrupoles are lenses with the focal length:

$$f = \frac{1}{k \cdot l_Q}, \tag{1.11}$$

with l_Q being the quadrupole magnetic field length. Hence, in synchrotrons, we have a lattice of quadrupoles, called FODO cells (**F** = focusing **O** = nothing (dipole, RF, ...) **D** = defocusing **O** = nothing (dipole, RF, ...).

For instance, each of the 8 LHC arcs consists of 23 FODO cells, each with 2 Quadrupoles, 6 Dipoles as well as additional instrumentation and corrector magnets that are installed in between for beam control.

Equation of motion

Hill's equation (first formulated in astronomy on orbital mechanics) is a differential equation for motions with periodic focusing properties. This same equation can describe the motion of particles in synchrotrons:

$$x''(s) - k(s)x(s) = 0, \tag{1.12}$$

where the restoring force is not constant, $k(s)$ is depending on the position s, and $k(s+L) = k(s)$ thus k is a periodic function, where L is the "lattice period". Hill's equation is describing a quasi-harmonic oscillation, where amplitude and phase depend on the position s in the ring.

Then the General solution of Hill's equation is:

$$x(s) = \sqrt{2J_x\beta(s)} \cdot \cos(\psi(s) + \varphi), \tag{1.13}$$

where $\beta(s)$ is a periodic function given by focusing properties of the lattice (the quadrupoles), and it is called: the β-function. J_x is called action, and it is the equation of an ellipse in the phase-space x, x'. φ is the initial phase of the particle.

In an actual accelerator ring, the β-function has small deviations $\Delta\beta$ from the design value. This is called β-beating $\frac{\Delta\beta}{\beta}$.

Although the articles are designed to travel along the design orbit, in reality, due to various errors like misalignment or field errors, they do not follow exactly the design (or reference) orbit, but another closed path, namely, the closed orbit.
Inserting (1.13) into the equation of motion (1.12), we get:

$$\psi(s) = \int_0^s \frac{ds}{\beta(s)}, \tag{1.14}$$

where $\psi(s)$ is the "phase advance" of the oscillation between point "0" and "s" in the lattice. For one complete revolution: number of oscillations per turn "Tune", or "Betatron Tune"

$$Q_y = \frac{1}{2\pi} \oint \frac{ds}{\beta(s)}. \tag{1.15}$$

The tune is important for the stability of motion over many turns. It has to be chosen appropriately, measured, and corrected. As there is a horizontal tune (Q_x) and a vertical tune (Q_y), the working point of a machine can be defined as the pair (Q_x, Q_y). In circular accelerators, particles pass through the same element every turn. Magnetic imperfections can lead to resonances and eventually deterioration of the beam. The working point has to be chosen away from these resonances.

The β-function essentially reflects the periodicity of the magnetic structure: 8 FODO cells mean that we have 8 oscillations of the β-function.

We can further define: $\alpha(s)$, $\gamma(s)$, which together with $\beta(s)$ are called the Courant-Snyder parameters or Optics parameters, and commonly referred to as the "Twiss parameters".

$$\alpha(s) = -\frac{1}{2}\frac{\beta'(s)}{\beta(s)}, \tag{1.16}$$

$$\gamma(s) = \frac{1 + \alpha(s)^2}{\beta(s)}. \tag{1.17}$$

These parameters allow describing and therefore controlling and manipulating the beam.

If we assume $s(0) = s_0$, $\psi(0) = 0$, $\beta(0) = \beta_0$ and $\alpha(0) = \alpha_0$, we get the transfer matrix with optics parameters:

$$M = \begin{pmatrix} \sqrt{\frac{\beta}{\beta_0}}(\cos\psi + \alpha_0 \sin\psi) & \sqrt{\beta\beta_0}\sin\psi \\ (\alpha_0 - \alpha)\cos\psi - (1 + \alpha_0\alpha)\sin\psi & \sqrt{\frac{\beta_0}{\beta}}(\cos\psi - \alpha\sin\psi) \end{pmatrix}. \tag{1.18}$$

This matrix is extremely useful because if we know α and β, we can compute the single-particle trajectories between two locations without remembering the exact lattice structure and strength of each element.

Going back to (1.13), J_x is called action and can be written as:

$$J_x = \frac{1}{2}\left(\gamma_x x^2 + 2\alpha_x x x' + \beta_x x'^2\right), \tag{1.19}$$

which is the equation of an ellipse in the phase-space x, x'. The shape and orientation of the ellipse are defined by the Courant-Snyder parameters, as they were previously defined.

At a given location:

$$x = \sqrt{2\beta_x J_x}\cos\psi_x, \tag{1.20}$$

the mean square value is:

$$\langle x^2 \rangle = 2\beta_x \langle J_x \cos^2\psi_x \rangle = \beta_x \langle J_x \rangle = \beta_x \varepsilon_x, \tag{1.21}$$

assuming that the action and the phase are uncorrelated, and uniform distribution in phase from 0 to 2π. Then, we can define the statistical emittance of a particle distribution:

$$\langle J_x \rangle = \sqrt{\langle x^2 \rangle \langle x'^2 \rangle - \langle x x' \rangle^2} := \varepsilon_x, \tag{1.22}$$

where ε_x is an intrinsic beam property that is defined at its creation.

Ideally, the distribution of particles in a bunch is Gaussian. Therefore,

$$\sigma_x = \sqrt{\langle x^2 \rangle} = \sqrt{\varepsilon_x \beta_x}, \tag{1.23}$$

describes the one σ beam size, or the envelope of all particle trajectories at a given position "s" in the storage ring, also referred to as "beam envelope"

$$\sigma_x = \sqrt{\varepsilon \beta_x}. \tag{1.24}$$

During acceleration, the emittance shrinks as a consequence of the adiabatic damping. When the longitudinal momentum is increased, the transverse remains constant. The action of the particles and therefore the emittance reduces as well. The net effect is called normalized emittance, defined as:

$$\varepsilon_n = \frac{\varepsilon}{\gamma}, \tag{1.25}$$

where γ is the Lorentz gamma, and it is unchanged during the acceleration.

1.1.3 Longitudinal Beam dynamics

There will only be a brief introduction to longitudinal beam dynamics, omitting many details. As stated previously, we need an electric field to accelerate the bunch of particles. What about the magnetic field during acceleration? As the equation of beam rigidity indicates, $B\rho$ should increase proportionally to the energy. Since the machine radius is constant, the dipole fields should increase accordingly. For the acceleration, RF cavities are used to apply the needed accelerating voltage on each passage. They gradually increase total energy by gaining a small amount each turn, or just maintaining a stable motion, to compensate for the losses during the last run.

As the accelerating voltage is changing with time, we need synchronization between beam and RF phase to gain energy. There is a synchronous RF phase, φ_s, for which the energy gain fits the increase of the field, as depicted in Figure 1.4. In addition, the particles do not feel the same voltage, as they arrive at different times, which means that they do not gain the same energy.

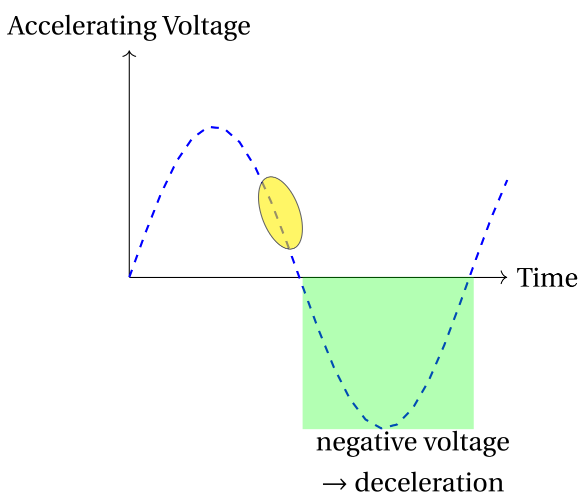

Figure 1.4: Acceleration and deceleration of the particle depending on when it arrives

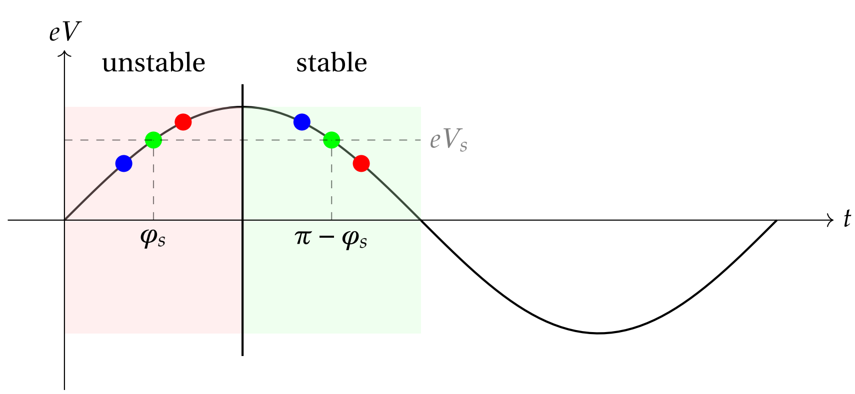

Figure 1.5: Stable and unstable region, based on when the particle arrives, in relativistic regime

In a relativistic regime $\gamma > \gamma_t$, an increase in momentum transforms into a longer orbit and thus a longer revolution time, as $\frac{p}{q} = B\rho$ indicates. With the help of Figure 1.5 we can deduce the following: The green particle is the synchronous particle, that has the perfect synchronous RF phase, then if another (not synchronous) gets into the cavity before the synchronous (blue particles), it will gain more energy, and as the beam rigidity dictates, it will get a longer orbit. If another not synchronous (red) particle, delays with respect to the synchronous, it will gain less energy, thus getting a shorter orbit. When $\omega_{RF}t = \varphi_s < \pi/2$, the non-synchronous particle will gradually move away from the synchronous, leading to an unstable situation. Thus, when $\pi/2 < \varphi_s < \pi$, the non-synchronous particles will move towards the synchronous, leading to a stable situation.

Like in the transverse plane, the particles are oscillating in longitudinal space. Particles are oscillating around the stable synchronous particle, varying phase and momentum. Typically, one synchrotron oscillation takes many turns (a lot slower than betatron oscillation). Therefore, the phase-space ellipse defines longitudinal emittance.

The so-called separatrix in the phase-space is the trajectory separating stable and unstable motion. The stable region is also called the RF bucket. Next, we can define the RF frequency, f_{RF}, that has to be a multiple of the revolution frequency f_{rev}:

$$f_{RF} = hf_{rev}, \tag{1.26}$$

where h is known as the harmonic number. This number defines the number of buckets, and each of them can be filled with an ion bunch, or it can be empty.

The linear synchrotron tune Q_{s0}, can be calculated using

$$Q_{s0} = \sqrt{\frac{-hqV_{RF}\eta\cos\varphi_s}{2\pi\beta_s^2 E_s}}, \tag{1.27}$$

where h is the harmonic number, q the particle charge, V_{RF} the RF voltage, η the phase slip factor, φ_s the phase of the synchronous particle, β_s the Lorentz beta and E_s the nominal particle energy.

1.1.4 Aknowledgments

The above is a short summary of the theory considered fundamental for this work, and it is mostly based on the knowledge gained from the lectures given by: Michaela Schaumann during the Summer Student Programme 2022 [31], Bernhard Holzer and Alexandre Lasheen [13] [15] during JUAS.

1.1.5 MAD-X

As written in the manual: “MAD-X is a general-purpose tool for charged-particle optics design and studies in alternating-gradient accelerators and beam lines. It can handle medium size to very large accelerators and solves various problems on such machines.”

All beam studies are performed using MAD-X.

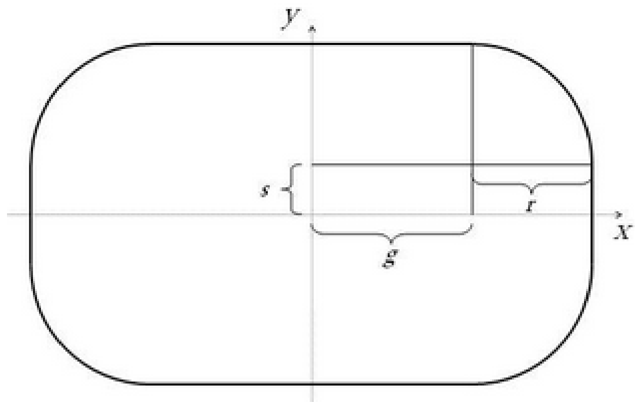

Figure 1.6: Aperture tolerances as defined in [12]

1.1.6 Apertures

In synchrotrons, apertures play a critical role in defining the physical boundaries, within which the particle beam must stay as it circulates through the accelerator. These apertures are essentially the limits set by the vacuum chamber and the magnetic and electrostatic elements of the synchrotron. The physical aperture is in general associated with the beam screen. A parameter closely connected to the aperture is the sum of the mechanical and alignment tolerances. The mechanical tolerance is the maximal error margin of errors in the element body which causes a decrease of aperture, and the alignment tolerance is a misalignment of the element in the accelerator, which also causes a decrease of aperture. The definition of aperture tolerances as defined in the MAD-X manual can be found in 1.6

Not to be confused with the physical aperture, dynamic aperture is defined as the minimum amplitude in phase space where the particle motion is unstable.

Chapter 2
Specific cases in the LHC

In this chapter, three specific cases in the LHC will be considered. Although each of them is unique and poses different problems, all three underline the need of defining a new, more systematic and flexible way of aperture data representation. It is highlighted that the full and accurate definition of the element's aperture is time-consuming and in some cases confusing and far from trivial or evident. Sometimes, it is inevitable not to go through the mechanical drawings.

2.1 TDIS studies

2.1.1 Overview

The TDIS is a component dedicated to the protection of the LHC equipment and was installed during LS2 in the vicinity of the injection from the Proton Supersynchrotron (SPS): in LSS2-L and LSS8-R. The new TDIS absorber consists of three modules, each of 1.565 meters long, and independently movable. Its full length is 5.740 m, as additional parts are needed to complete the full component. The TDIS replaces the old TDI, a single unit measuring just over four meters, as an upgrade to HL-LHC beam parameters, to overcome several operational issues that had been reported during the TDI's operation. More specifically, to reduce RF heating, deformation, and vacuum spikes, improve materials and operational aspects. The three modules of the TDIS are two collimator-like jaws. [9]. A summary of TDIS issues can be found here [5, 10, 11].

The operating scenario for the TDIS can be summarized as follows. When injecting with pilot bunches, the jaws are kept at a "relaxed position", ±10 mm apart from the beam center. At intermediate intensity (with 12 nominal bunches) the jaws have to be aligned to the circulating beam, and positioned at a nominal setting of $\approx \pm 4$ mm with respect to the beam's closed orbit. Then, at the injection of nominal bunches, the jaws are locked to the required nominal position. Once the injection process is completed and the kicker magnets (MKIs) are set to standby mode, the jaws can be opened to the parking position, meaning that they are fully opened and at the maximum distance from one another ($\approx \pm 55$ mm).

The below chapter is a brief summary of the documentation available in EDMS [22]. First, a brief description of the geometry of TDIS as it appears in the EDMS drawings and LDB. The gathered aperture information will be combined using MAD-X to conduct beam aperture studies inside the TDIS.

2.1.2 Aperture variations along the TDIS

Data from the Layout DB and overview of the TDIS

The TDIS is consisted of different parts, and each of these installed parts is registered in LDB. Nonetheless, most of them, whose names start with V (implying the word vacuum), are not needed for beam aperture studies because they are outside the beam path. The vacuum elements relevant for the apertures are only the vacuum valves, which will be discussed shortly, as they impose some aperture changes.

Looking for the TDIS.A4L2 in LDB, one can find a collapsing list (as in Figure 2.1) with all the parts belonging to the item. The system followed in LDB is hierarchical, as also the collapsing list implies, meaning that different parts inherit their position directly from the element above it in the hierarchy.

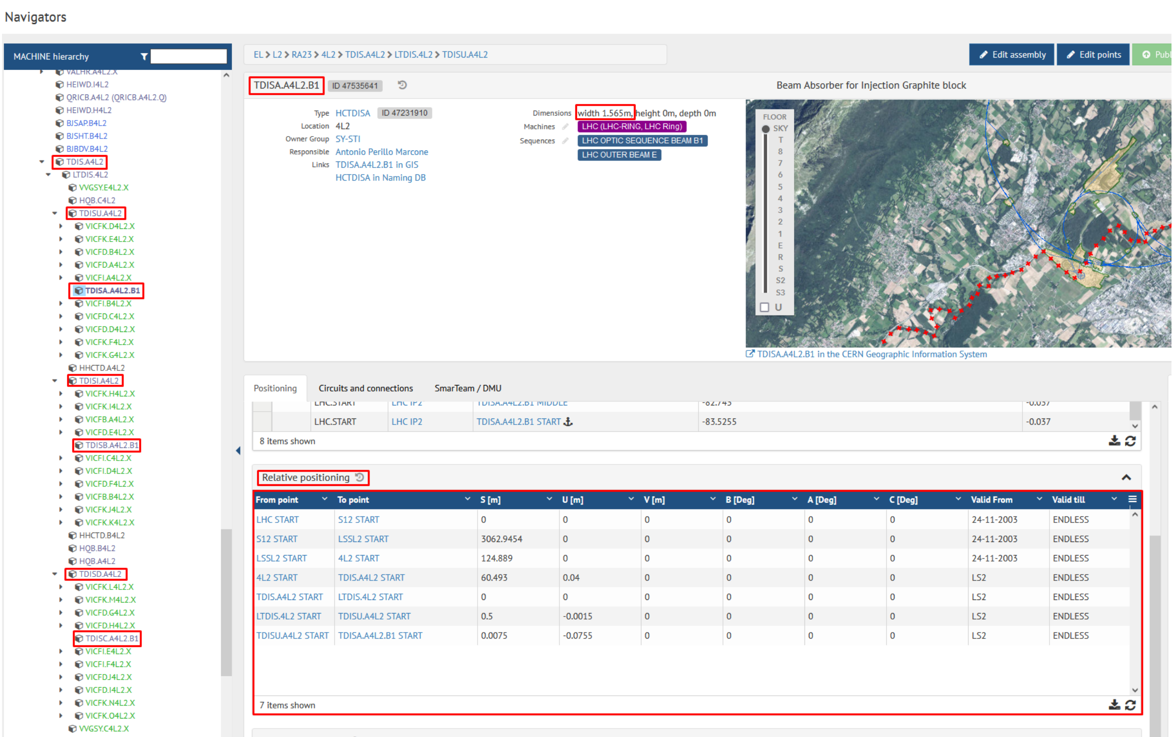

Figure 2.1: Screenshot of LDB website. On the left, the collapsing list of the parts in hierarchical order is visible. In the middle down, there is the relative positioning system bar menu

In LDB, the (U, V, S) coordinate system is used, representing the transverse (U, V) and longitudinal position (S) of a specific point of the element's (e.g. START) relative reference path. At U = 0, there is the so-called "mid beam" reference (an imaginary beam trajectory), that sits in the middle of Beam 1 and Beam 2 reference orbits. It should be noted that the first vacuum valve of the TDIS is also in alignment with this mid-beam.

The (U, V, S) coordinates are essential to correctly interpreting the mechanical drawing, extracting the aperture information and finally reconstructing the aperture model.

In order to facilitate the process, it is useful to divide the TDIS into 5 subsections and to have an overview of the physical structure of the main parts of the TDIS. At first, there is the vacuum valve, namely VVGSY (numbers 1 and 5 in Figure 2.2), this part is in the entrance and the exit of the TDIS (these two are identical in shape, but they are positioned mirrored to one another, in the same way that the injection regions to the LHC are). Next, there is the aperture transition part (numbers 2 and 4), there are two parts (transition 1 and transition 2) after the vacuum valve in the beginning and before the vacuum valve in the end (these transition parts are not identical). Finally, there are the main parts of the TDIS, the 3 modules, which have clear similarities, but they are not completely identical.

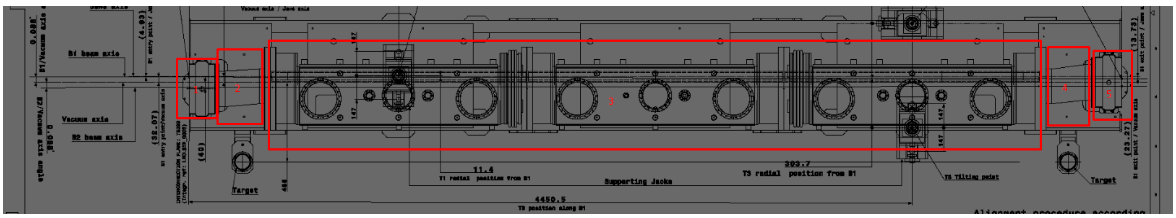

Figure 2.2: TDIS seen from the side, IP2 is to the right when one is moving clockwise on the LHC ring. The five distinct parts of the TDIS.

Aperture of Transition Parts There was an effort to validate and cross-check the data offered in the mechanical drawings and LDB data, which in some cases revealed some missing or incorrect data. An indicative example is the transition parts, as the transition functional position was missing from LDB. Since this part has a complex aperture, it could not be added without approximations in LDB because it did not comply with any existing aperture shapes. The process is documented in detail in [22].

2.1.3 Aperture with beam

TDIS before IP2

Below, the beam sizes are simulated at the end of the first jaw of the TDIS. Injection optics at 450 GeV are used, and the beam sizes are plotted at 1σ, 6.5σ and 12.6σ. The exact location of the beam is at $s = -83.5255$ m, with respect to IP2. Note: The experimental spectrometers are off, they are not needed for these simulations.

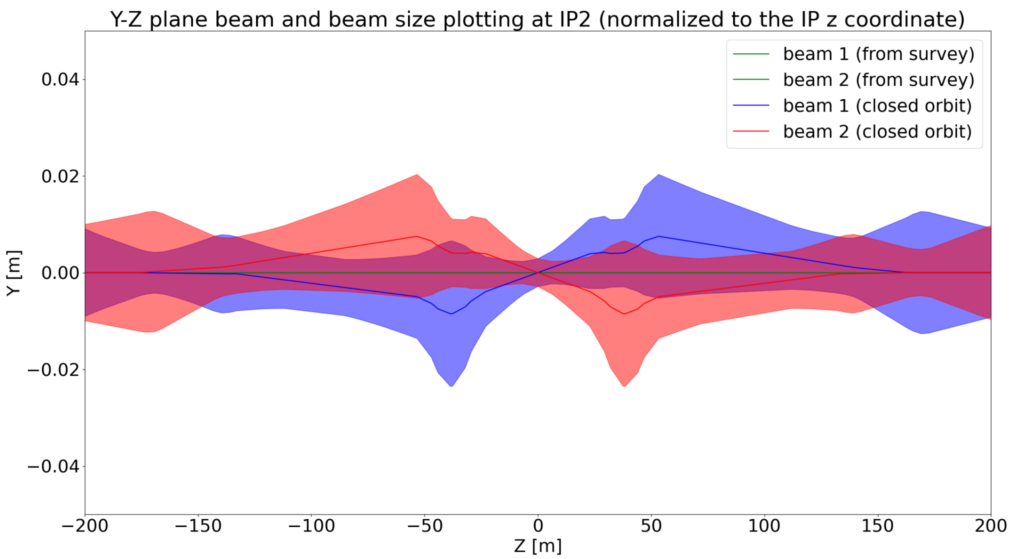

Figure 2.3: Z-Y plane at IP2, the beam sizes are plotted at 12.6σ. The reference beams from survey as well as the closed orbit are plotted.

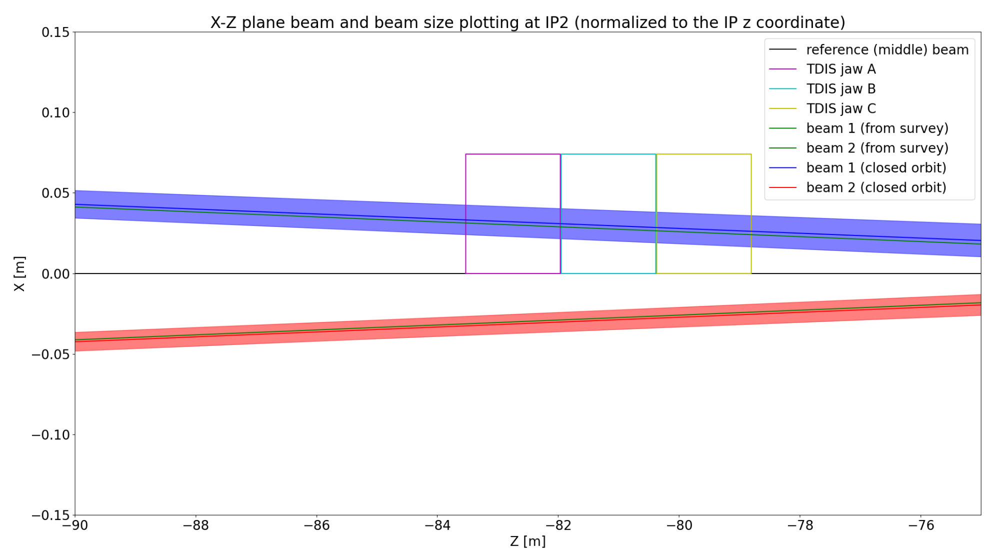

Figure 2.4: X-Y plane at the position of the TDIS, the jaws are indicated with colors. The beam sizes are plotted at 12.6σ. The reference beams from survey as well as the closed orbit are plotted.

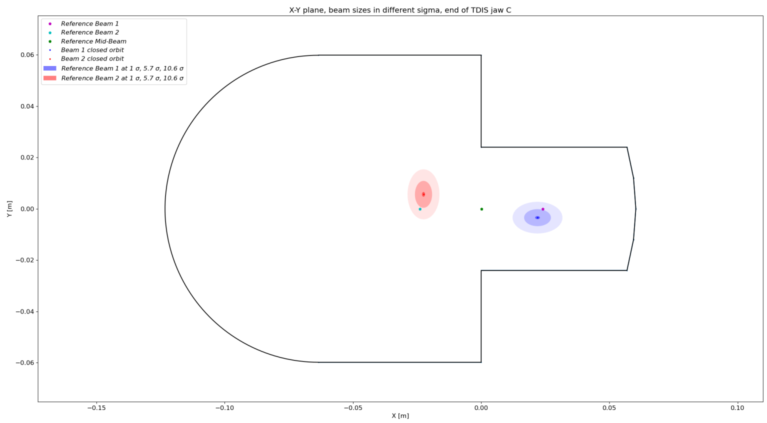

Figure 2.5: Aperture on X-Y plane at the end of the TDIS jaw C

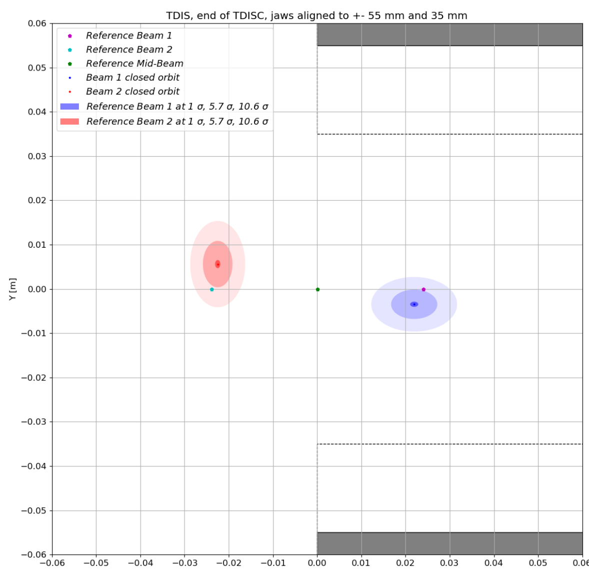

Figure 2.6: X-Y plane at the end of the TDIS jaw C, the jaws are indicated at ±55 and ±35 mm.

TDIS after IP8

Then, the beam sizes are simulated at the end of the first jaw of the TDIS after IP8. The same optics and parameters are used. The exact location of the beam is at s = + 82.743 m, with respect to IP8. Note: The experimental spectrometers are off, they are not needed for these simulations.

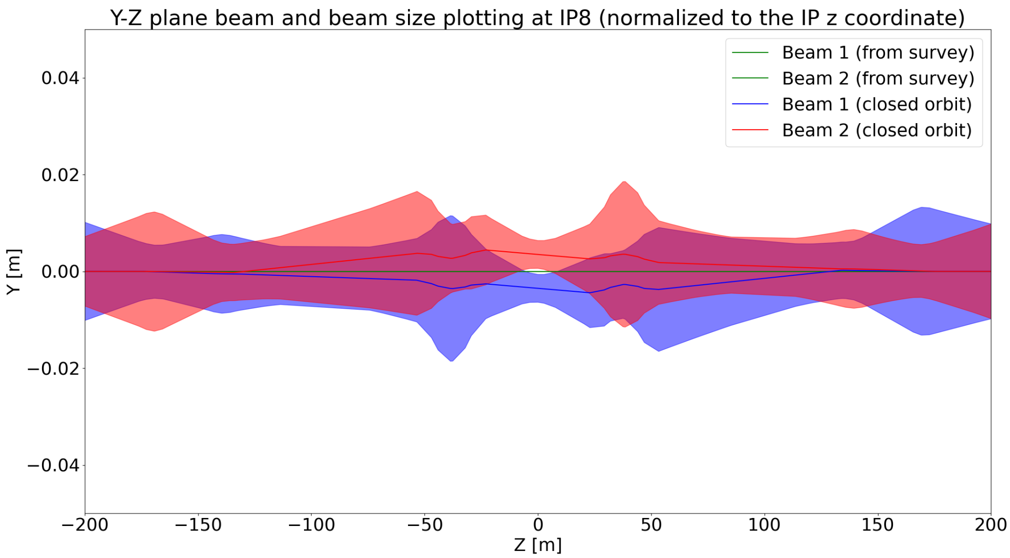

Figure 2.7: Z-Y plane at IP8 (normalized to it)

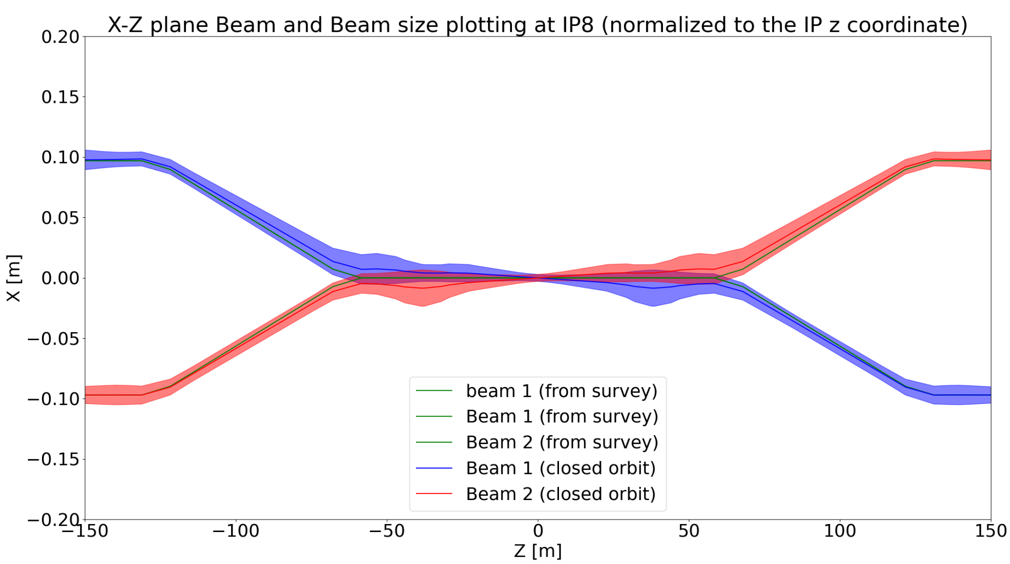

Figure 2.8: Z-X planes at IP8 (normalized to it)

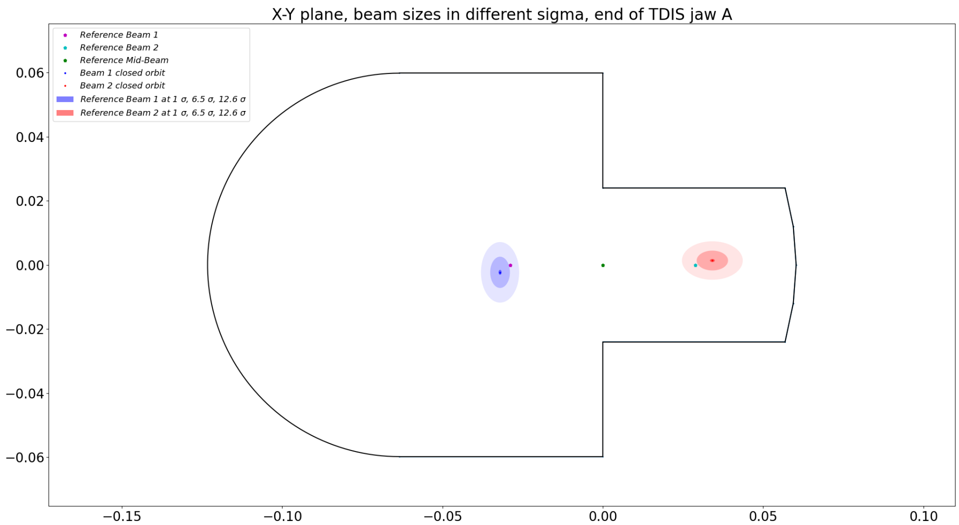

Figure 2.9: X-Y plane at the end of the TDIS jaw A. In operational position, the jaws are closed to cut part of the beam

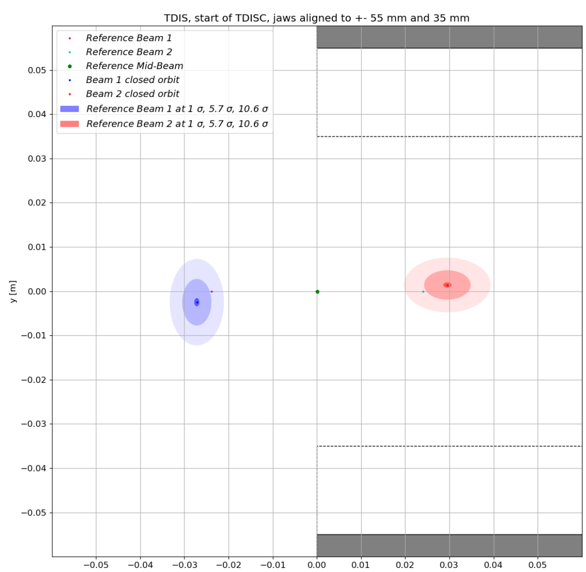

Figure 2.10: X-Y plane at the end of the TDIS jaw A, the jaws are indicated at ±55 and ±35 mm.

2.1.4 Comments

Overall, the functional position of the TDIS, where found, was correct and useful. The aperture information in many cases was too coarse or incomplete to be usable for accurate beam studies.

As LDB can, in fact, contain all the sufficient information for beam studies, in particular, if it can also store complex shapes (where there are real beam losses in the machine). The Layout drawings contain only a side view and not a top view and do not show beam references and apertures in a systematic and comprehensive way. Therefore, the Layout drawings need complements (such as equipment drawings and 3D models) to obtain data needed in layout DB. Additionally, it is true that the drawings arrive too late in the ECR (Engineering Change Request) and installation processes, and/or there are no sufficient iterations to quote the values needed. Finally, although EDMS DXF output, PLM viewer, and STEP files were essential to carry out the work, the 3D models are unusable for precision measurements. As a result, such a process is extremely time-consuming and prone to errors.

2.1.5 Proposals

As stated before, the transition functional position is not defined in LDB, also it has a complex aperture that cannot be added to LDB because it does not comply with any existing aperture. One idea would be to approximate it with a polygon, but that would be cumbersome and time-consuming, without giving any good precision. Instead, a good solution would be to specify the path using an SVG image, because the SVG standard:

1. allows a concise, human-friendly, text-base description of any path

2. is a widely used standard, is web-friendly, plenty of free editors

It would, overall, be a useful addition to the set of aperture shapes in LDB and the same to be supported in MAD-X.

2.1.6 Actions taken

The dimensions for transition 1 are based on the information found in drawing LHCTDIS_0206 [38], from EDMS. Transition 1 is identical for both TDIS in IP2 and IP8. For transition 2, based on the drawings, the aperture is identical in shape only. What does change is the position of it (U, V coordinates). Hence, the above SVG represents both of the above apertures. For reference, the most useful drawing for transition 2 is: LHCTDIS_0227 [39].

As decided, the aperture for the TDIS modules is defined at parking position (which is the same for all three jaws) at $\pm 55mm$, as shown in [18]. The apertures in the equivalent modules are the same, both TDIS IP2 and TDIS IP8.

For these shapes, 2 drawings were used: LHCTDIS_0254 [40] (the most useful of the two, although it is still a draft) and LHCTDIS_008, [37], although the information retrieved from this drawing can be found in several others. More precisely, in the second drawing, there were some tolerances in the gap between the RF screen and the jaws, precisely 4 ± 0.1 mm. The tolerances in this case were neglected. The second and last dimension taken from this file is the distance between the jaws and the RF wall, 4.5 mm. For the horizontal length of the jaws, it is considered 62 mm

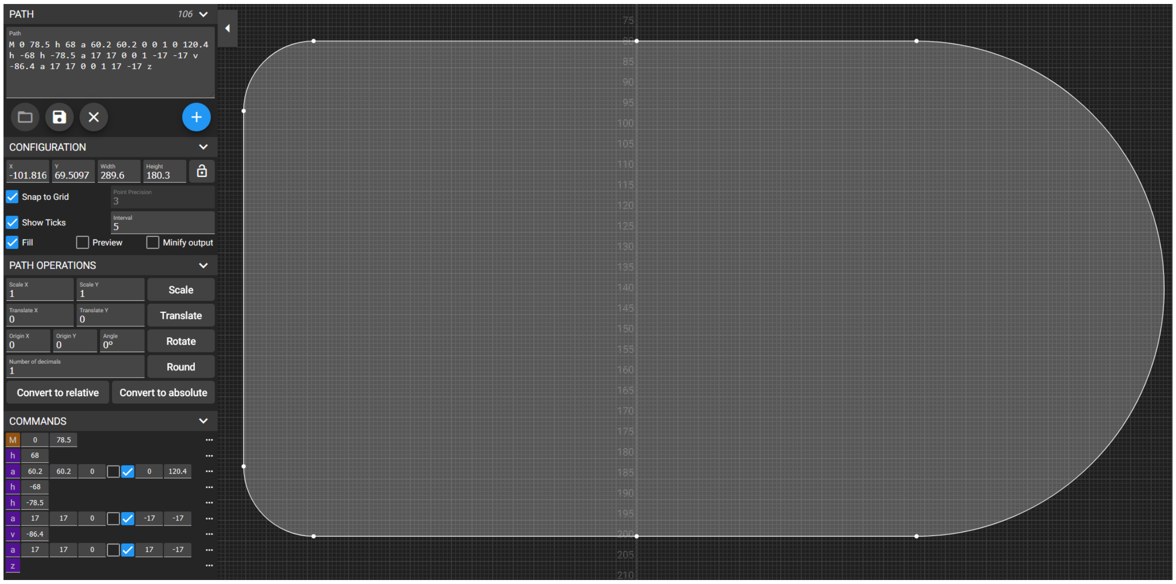

Figure 2.11: The aperture of the inner part of the two transition parts of TDIS, in SVG format, in the environment of the used web app. The path used to create the above shape is: `M 68 60.2 a 60.2 60.2 90 0 0 0 -120.4 h -68 h -61.5 a 17 17 90 0 0 -17 17 v 86.4 a 17 17 90 0 0 17 17 h 61.5 z` [36].

Figure 2.12: Aperture of the modules of the TDIS at parking position $\pm 55mm$. SVG path: `M 0 4 h 78.4 a 60 60 0 0 1 0 120 h -78.4 h -4 v -5 h -62 v 5 h -4.5 v -120 h 4.5 v 5 h 62 v -5 z` [35]

overall, as [40] suggests. Finally, two variants were defined with different apertures: `LHCTDIS_0006` (Layout DB type TDIS_T_0006) and `LHCTDIS_0188` (Layout DB type TDIS_T_0188).

Note: C is a rotation around the vertical axis V, B around the S axis and A around the U axis. There rotations are clockwise. A, B, C rotations are commonly mostly used in LDB.

The transitions for the TDIS were implemented as follows:

For TDIS.A4R8: The transitions were inserted with a rotation on $A = 180°$, consistent with the other subassemblies. In the direction of Beam 1, transition 1 (drawing LHCTDIS_0006) takes the assembly from $u = 0$ to $u = 0.02485$. Subsequently, transition 2 (drawing LHCTDIS_0188) extends the assembly from $u = 0.02485$ to $u = 0.040$. [24]

For TDIS.A4L2: The transitions were inserted with a rotation on $A = 0°$. In the direction of Beam 1, transition 2 (drawing LHCTDIS_0188) adjusts the assembly from $u = 0.040$ to $u = 0.01515$. Following this, the transition 1 (drawing LHCTDIS_0006) completes the assembly from $u = 0.01515$ to $u = 0$.

These changes were possible with the help of Joao Oliveira and Bruno Feral (from EN-ACE), they are the ones to validate and insert in LDB the new data.

2.2 TCLIA studies

This section provides an overview of the TCLIA studies to mitigate the misalignment issue that occurred during LS2. The aperture of the TCLIA is also defined. The full document is available on EDMS, [21].

2.2.1 TCLIA general description

After the vertical magnet kickers (MKIs), are used to inject the new bunches from the SPS into the LHC closed orbit, a system of a beam stopper, or collimator, (TDIS) and two auxiliary collimators (TCLIA and TCLIB) are installed in each injection region for protection, to intercept the miskicked beams in case of MKI malfunctioning [30].

The TCLIA collimator's jaws are set at an aperture of $\pm 7.3\sigma$ (plus and minus signs for the upper and lower jaws respectively) from the center of the Beam, at the nominal LHC emittance of $\epsilon = 3.5\mu m$ during the injection process. After the injection is completed and the MKIs are in standby mode, the collimator's jaws are opened to parking position (maximum aperture), not to present anymore an aperture bottleneck. The maximum aperture at the parking position is $\pm 28mm$ (with the current optics).
For completeness, TDIS has a jaw gap of $\pm 6.8\sigma$, while TCLIB has $\pm 8.3\sigma$, in comparison to the TCLIA that has $\pm 7.3\sigma$.

2.2.2 TCLIA.4R2 modifications during LS2

In order to increase the acceptance of ALICE ZDC to be compatible with 50 ns Pb ions bunch spacing (the new baseline for HL-LHC Pb-Pb collision), the maximum gap of the TCLIA.4R2.B1 had to be increased, and the TCLIA collimator had to be displaced 2.2 m closer to IP2 (ALICE) [30].

The actions taken can be summarized as follows: The TCLIA was removed and modified to increase the maximum gap by $\approx$ 3 mm between the two beams. The vacuum layout in LSS2 was also modified to allow for the displacement of TCLIA 2.2 m closer to IP2. Finally, the modified TCLIA was installed and aligned at the new position, followed by the vacuum connection and bake-out.

The maximum aperture and longitudinal position of the TCLIA.4R2.B1 have an impact on the acceptance of the Zero-Degree-Calorimeter (ZDC) of ALICE. The TCLIA blocks the acceptance of the ZDC posing a limit in the maximum allowed crossing angle. More information can be found in [14].

To cope with the above new requirements, modifications of the TCLIA.4R2 hardware and the IR2 vacuum layout had to be carried out.

The TCLIAs installed in the LHC have been designed and commissioned to allow a full opening of 56 mm during operation. To increase the maximum opening without modifying the design, the setting of the mechanical end-stops and the related end-of-stroke switches can be pushed to their physical limits. A test on the surface (not in a tunnel) on the spare TCLIA collimator confirmed the gain of 3 mm in aperture, to go to 59 mm, respecting safe hardware operation. Therefore, the collimator could approach the IP by 2.2 m. The displacement of the TCLIA by 2.2 m also had an impact on the A4R2 vacuum sector.

2.2.3 Problems because of the modification

Observations in Loss Maps, Figure 2.13, after the modification (in Figure 2.14), first indicated large unexpected losses in IR2 and a potential issue. The black lines indicate the collimators, below the arrow it's TCLIB and on the left of it, there is TCLIA. The blue lines indicate the apertures. The losses downstream indicated the misaligned jaw of the TCLIA. TCLIA was opened at 6.8σ jaw gap when performing the lossmap.

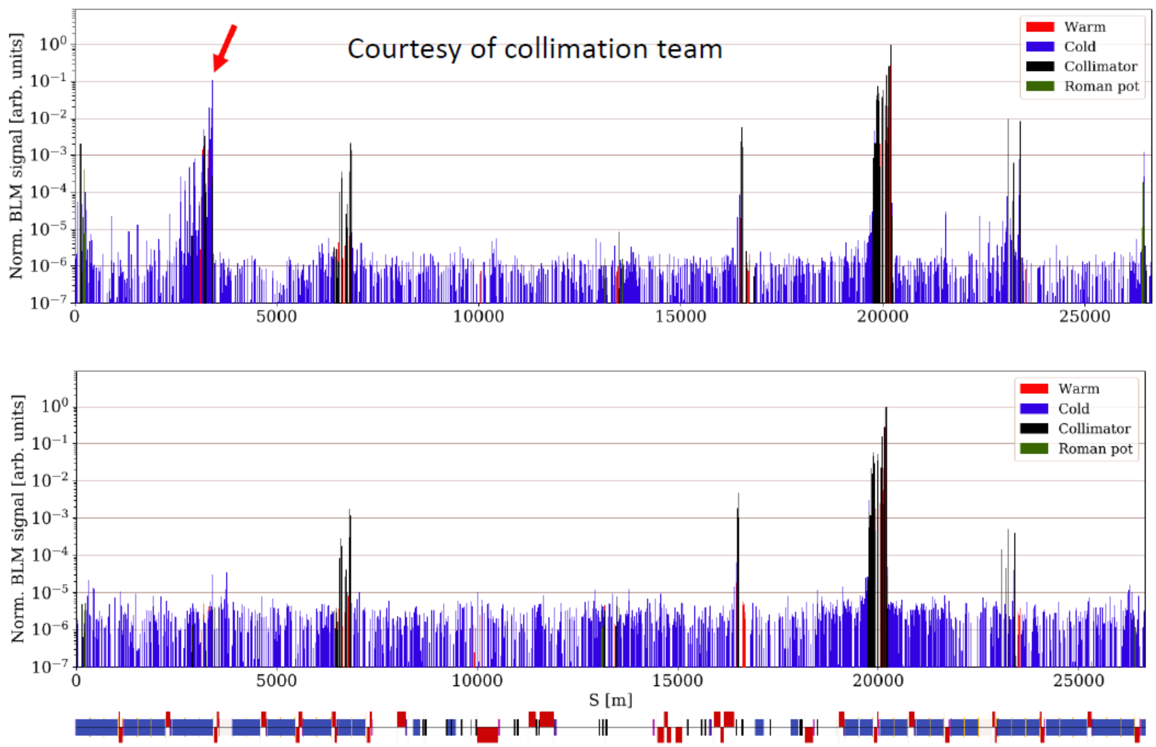

Figure 2.13: Horizontal loss maps for Beam 2 only. The injection protection is in, in both images. In the lower image: the lower jaw of TCLIA.4R2 is additionally retracted by 5 mm, [7], [29].

Despite a small expected reduced margin in the distance between Beam 2 and the TCLIA jaw, the losses were much higher than anticipated. Because TCLIA was aligned incorrectly, a transverse shift of $\approx 3.3mm$ towards Beam 2 was introduced, reducing the distance from the jaw to $\approx 200\mu m$, [8], that induced the high losses.

The displacement by 2.2 m reduced the minimum separation between the two beams by 3.37148513 mm (both at the entrance and exit, the divergence comes at the 11th decimal point). Based on data from Geode, no change in RST parameters or orbit bump was introduced, therefore the TCLIA was displaced in parallel to Beam 1 and not the mid-Beam. The second was supposed to be done and it was initially assumed that it has been done correctly. A summary of the situation is presented in Figure 2.15. Thus, also a transverse displacement was applied, and not just a longitudinal, as it was supposed to.

As a temporary solution, to mitigate the losses on Beam 2, the lower jaw proposed to be opened to 13.6σ (13.6σ down from the center of Beam 1). The change in the opening of the TCLIA lower jaw does not change the protection guaranteed by the injection protection system in case of MKI failure.

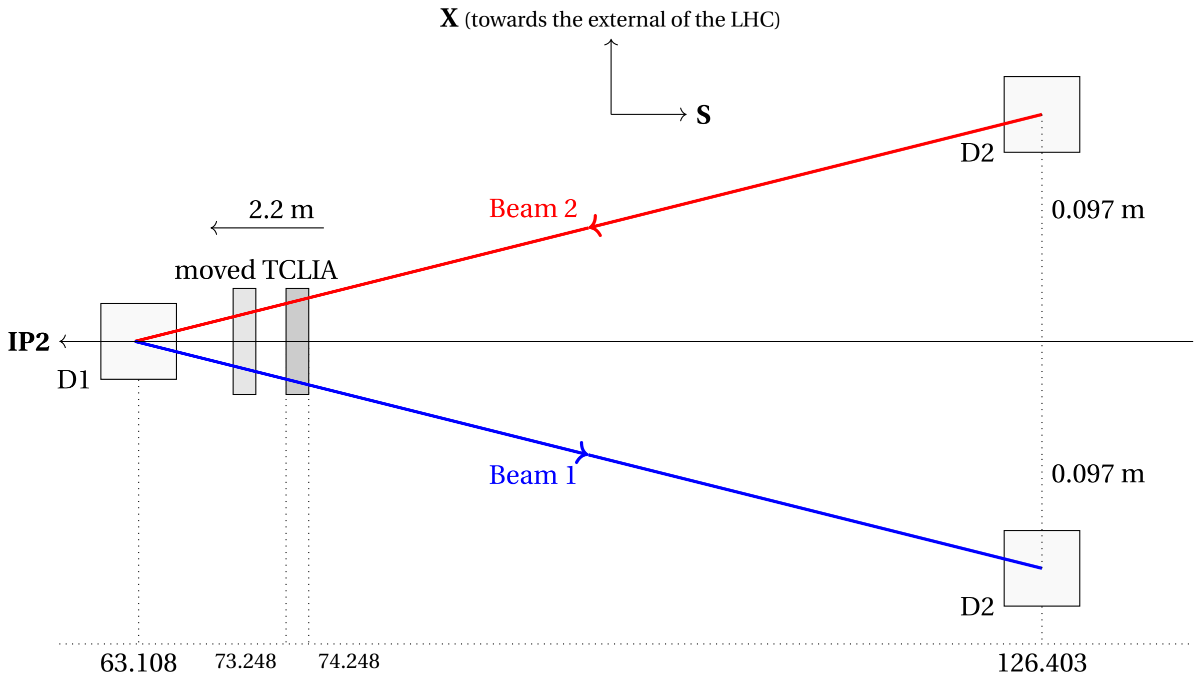

Figure 2.14: Geometric distance between Beam 1 and Beam 2 (reference orbits) as determined by the D1 and D2 magnets in IR2 where the TCLIA is installed [8]

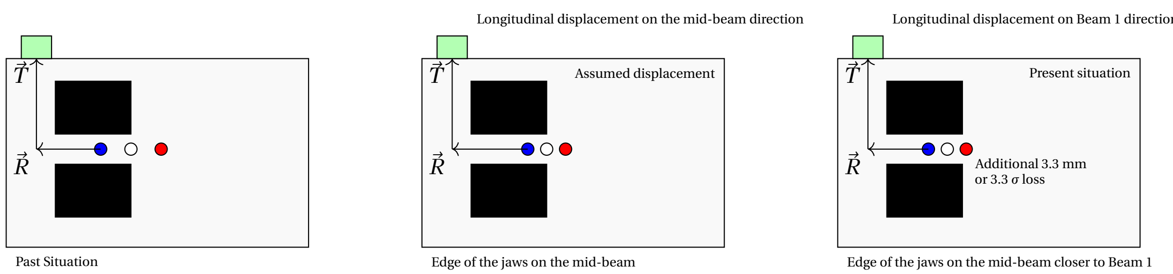

Figure 2.15: Geometric distance between Beam 1 and Beam 2 as determined by the D1 and D2 magnets in IR2 where the TCLIA is installed [19]

2.2.4 Beam and optics studies

For the below studies, a summary of all the relevant beam parameters is presented, at the entrance and exit of the TCLIA, followed by the corresponding plots.

For the LHC studies, the nominal emittance of $\epsilon_N = 3.5 \mu m$ was used.

TCLIA	2018	2022 (incorrectly aligned)	2022 if correctly aligned (positive separation sign)	2023 negative separation sign (still incorrectly aligned)
TCLIA Cumulated distance from IP2 entrance [m]	73.248	71.048	71.048	71.048
TCLIA Cumulated distance from IP2 exit[m]	74.248	72.048	72.048	72.048

Table 2.1: TCLIA entrance and exit distances from IP2

TCLIA entrance	2018	2022 (incorrectly aligned)	2022 if correctly aligned (positive separation sign)	2023 negative separation sign (still incorrectly aligned)
Reference Beam 2 (x/y) [mm]	15.539/0	12.167/0	12.167/0	12.167/0
Reference Beam 1 (x/y) [mm]	-15.539/0	-12.167/0	-12.167/0	-12.167/0
B1 closed orbit (x/y) [mm]	-14.040/6.020	-10.633/6.185	-10.633/6.185	-15.592/6.186
B2 closed orbit (x/y) [mm]	12.790/-3.792	9.311/ -3.923	9.311/ -3.923	12.078/-3.923
B1 ref orbit (x/y) (tw.x/tw.y) [mm]	1.498/6.020	1.534/6.1852	1.534/6.1852	-3.424/6.185
B2 ref orbit (x/y) [mm]	-2.748/-3.792	-2.856/-3.923	-2.856/-3.923	-0.089/-3.923
β_x / β_y of B1 [m]	52.945/129.816	55.994/136.391	55.994/136.391	55.994/136.391
β_x / β_y of B2 [m]	129.816/52.945	136.391/55.994	136.391/55.994	136.391/55.994
Maximum beam size (x/y) at 1 σ [mm]	0.973/0.621	0.997/0.639	0.997/0.639	0.9976/0.6392
Maximum beam size (x/y) at 5.7 σ [mm]	5.547/3.543	5.686/3.643	5.686/3.643	5.6866/3.6436
Maximum beam size (x/y) at 10.6 σ [mm]	10.317/6.588	10.575/6.775	10.575/6.775	10.575/6.775
10.6 σ horizontal envelope distance from jaw [mm]	2.4733	-4.6354	-1.2639	-1.868
5.7 σ horizontal envelope distance from jaw [mm]	7.2426	0.2531	3.6245	3.0203

Table 2.2: Beam parameters at the entrance of TCLIA

notes:

1. As beam size is considered the distance from the beam center (and not the double of that), in the indicated σ region.
2. The spectrometers for this study are off, as they don't affect it.
3. A negative distance indicates that the beam is hitting the jaw.

TCLIA exit	2018	2022 incorrectly aligned	2022 if correctly aligned (positive separation sign)	2023 negative separation sign (still incorrectly aligned)
Reference Beam 2 (x/y) [mm]	17.072/0	13.700/0	13.700/0	13.700/0
Reference Beam 1 (x/y) [mm]	-17.072/0	-13.700/0	-13.700/0	-13.700/0
B1 closed orbit (x/y) [mm]	-15.589/5.945	-12.182/6.110	-12.182/6.110	-17.083/6.110
B2 closed orbit (x/y) [mm]	14.3726/-3.732	10.893/-3.863	10.893/-3.863	13.597/-3.863
B1 ref orbit (x/y) (tw.x/tw.y) [mm]	1.4824/5.945	1.518/6.110	1.518/6.110	-3.382/6.110
B2 ref orbit (x/y) [mm]	-2.699/-3.732	-2.807/-3.863	-2.807/-3.863	-0.104/-3.863
β_x / β_y of B1 [m]	51.647/126.906	54.576/133.373	54.576/133.373	54.576/133.373
β_x / β_y of B2 [m]	126.906/51.646	133.373/54.576	133.373/54.576	133.373/54.576
Maximum beam size (x/y) at 1 σ [mm]	0.962/0.614	0.986/0.631	0.986/0.631	0.9865/ 0.6310
Maximum beam size (x/y) at 5.7 σ [mm]	5.485/3.499	5.623/3.597	5.623/3.597	5.6234/3.5972
Maximum beam size (x/y) at 10.6 σ [mm]	10.201/6.507	10.457/6.689	10.457/6.689	10.4576/6.6895
10.6 σ horizontal envelope distance from jaw [mm]	4.171	-2.9358	0.4356	-0.2321
5.7 σ horizontal envelope distance from jaw [mm]	8.887	1.8983	5.269	4.6020

Table 2.3: Beam parameters at the exit of TCLIA

In the last row of both Table 2.2 and Table 2.3, the distance from the bottom jaw to the nearest point inside 5.7σ beam envelope is shown. The minus sign indicates that the beam region of 10.6σ is hitting the jaw, thus the particles there are lost. Hence, after the TCLIA misalignment, there is a clear problem, especially at the entrance, as the beam at 5.7σ is too close to the jaw.

The case of the changed separation sign is also presented in the Tables, to facilitate the comparison between the situations, but it will be covered in the following subsection.

Given the below beam size and position plots, the reduced margin between Beam 2 and the lower jaw due to the displacement is evident.

note: For all the cases below, the jaws are opened at 7.3σ.

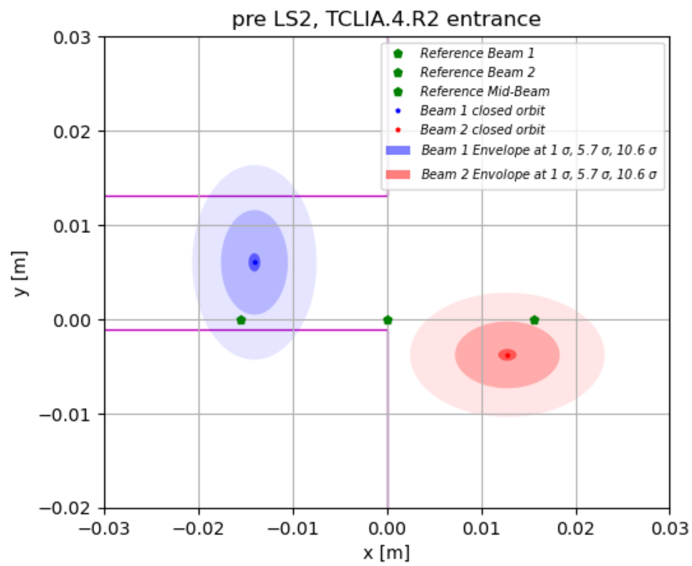

Figure 2.16: Pre LS2 situation, TCLIA entrance, jaws opened at 7.3σ

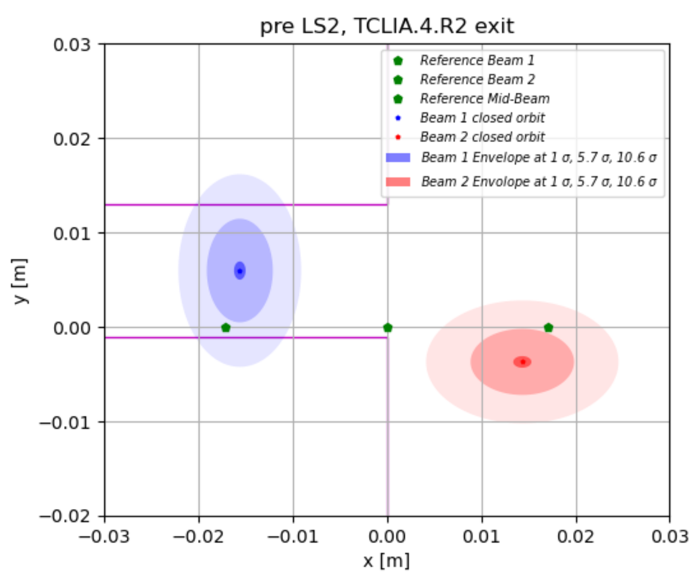

Figure 2.17: Pre LS2 situation, TCLIA exit, jaws opened at 7.3σ

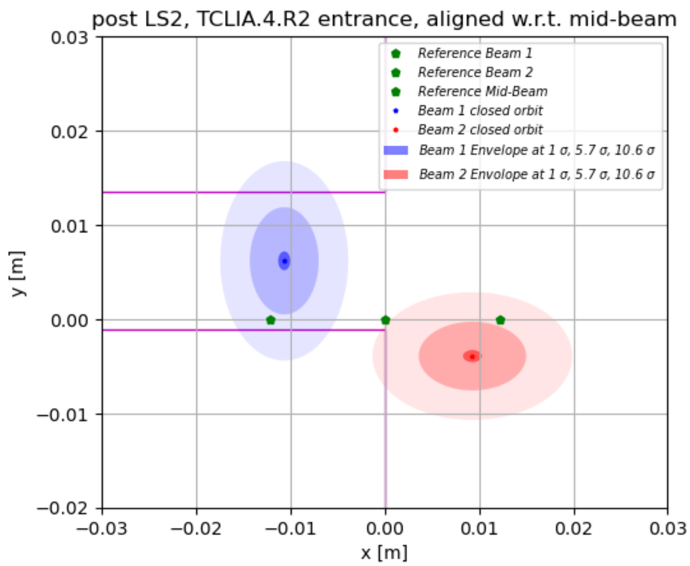

Figure 2.18: Post LS2, TCLIA entrance, correct alignment (with respect to the mid-beam)

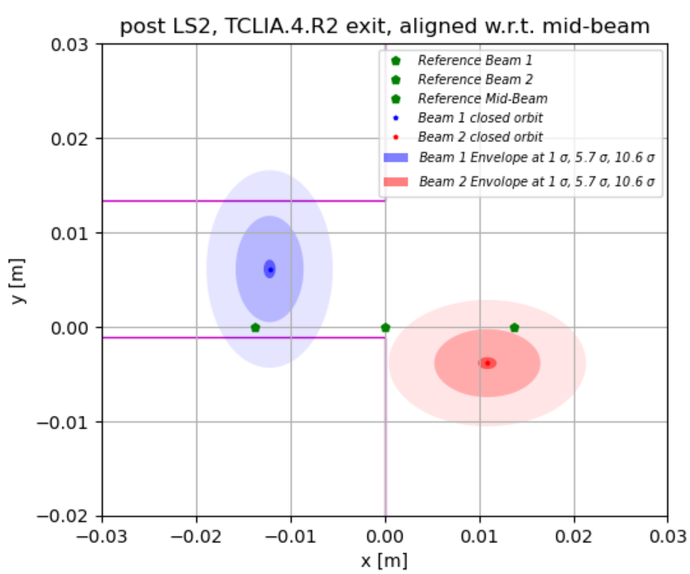

Figure 2.19: Post LS2, TCLIA exit, correct alignment (with respect to the mid-beam)

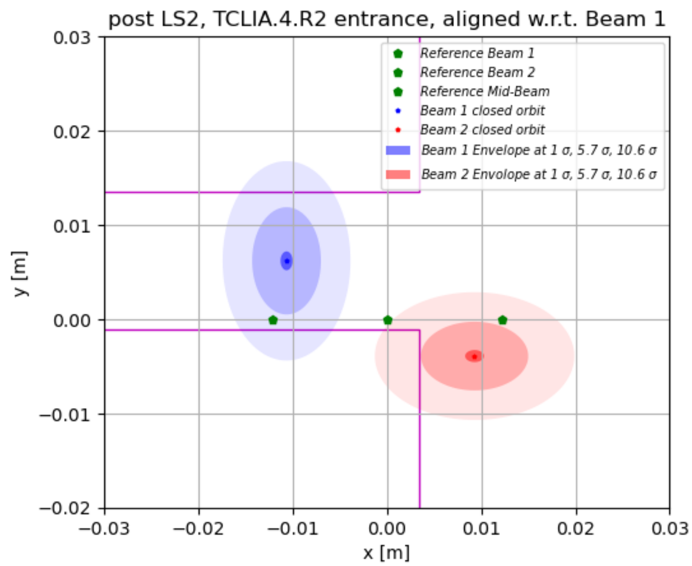

Figure 2.20: Post LS2, TCLIA entrance, incorrect alignment (with respect to the Beam 1)

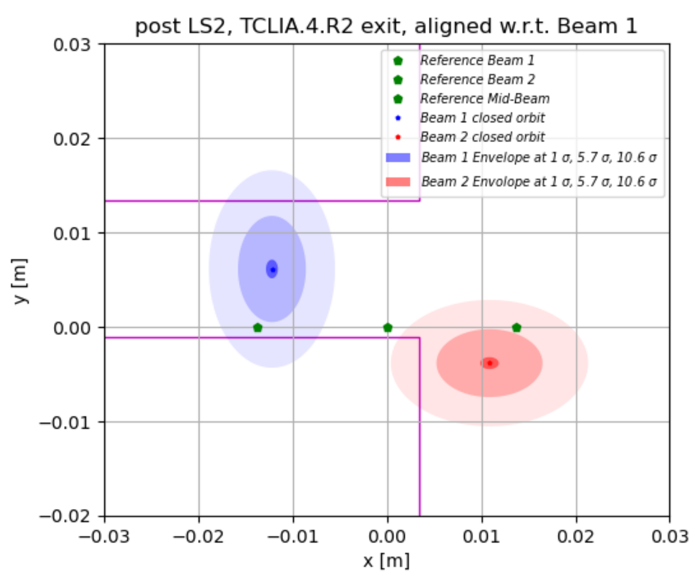

Figure 2.21: Post LS2, TCLIA exit, incorrect alignment (with respect to the Beam 1)

Sign inversion

As a proposed solution, a change of separation sign can increase the margin distance from Beam 2 to the bottom jaw. This would also increase the MCBXH current needs that is also used to correct for triplet misalignment and D1 transfer function errors.

The change of the separation sign has to be done at the beginning of the commissioning process and should not change until its end.

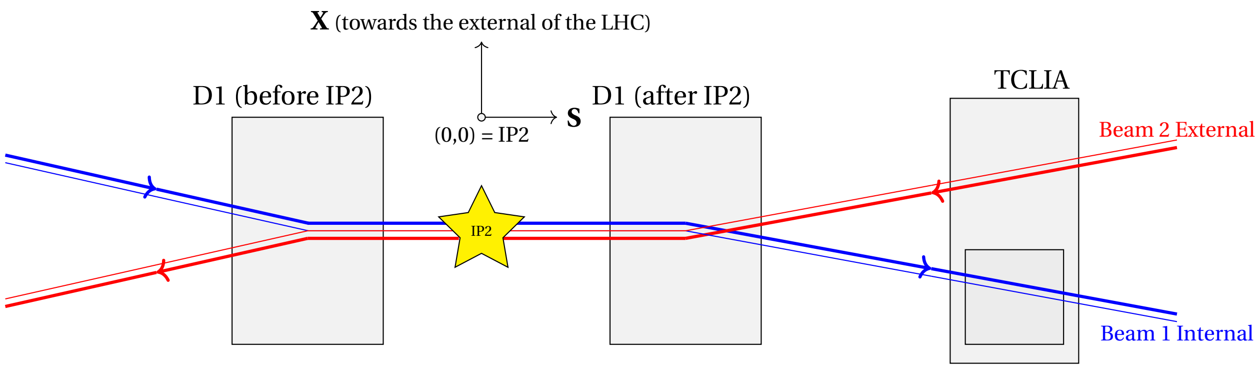

Figure 2.22: The separation sign is positive since Beam 1 offset is positive at the IP. This was the configuration for 2022, Beam 2 is closer to the jaws.

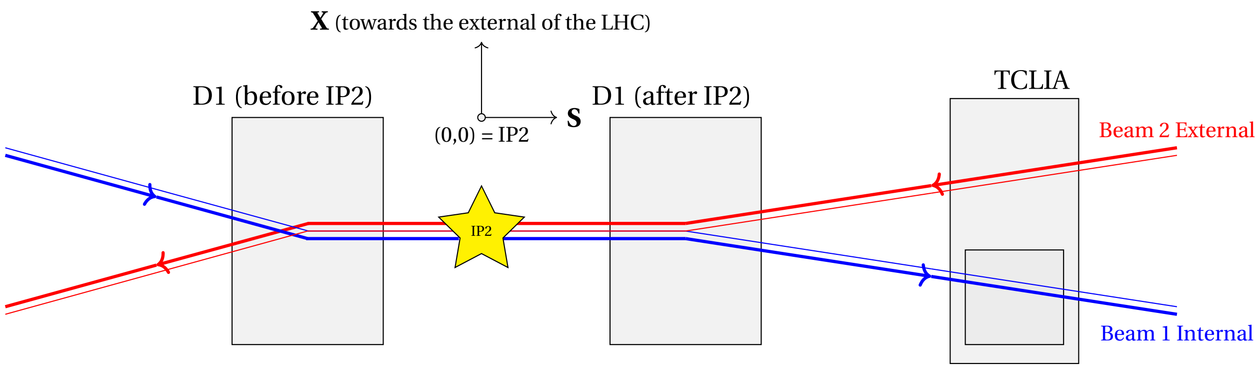

Figure 2.23: The separation sign is negative since Beam 1 offset is negative at the IP. This is the configuration for 2023, Beam 2 is further from the jaws.

The change of the separation sign can indeed considerably take Beam 2 apart from the bottom jaw, providing a $3.0203mm$ and $4.6020mm$(at 5.7σ at the entrance and the exit respectively) safety margins from the jaws, without compromising the overall performance. The minor drawback is the increase in the MCBXH current needs.
It should lastly be noted that, for the inversion of the separation sign, beams checks have ensured that TDIS is not creating an aperture bottleneck.

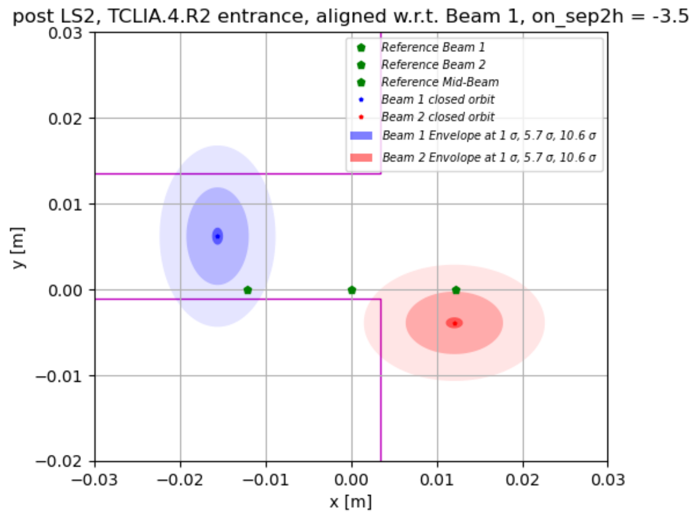

Figure 2.24: Post LS2, TCLIA entrance, still incorrectly aligned. Here, the separation sign (on_sep2h) is inversed.

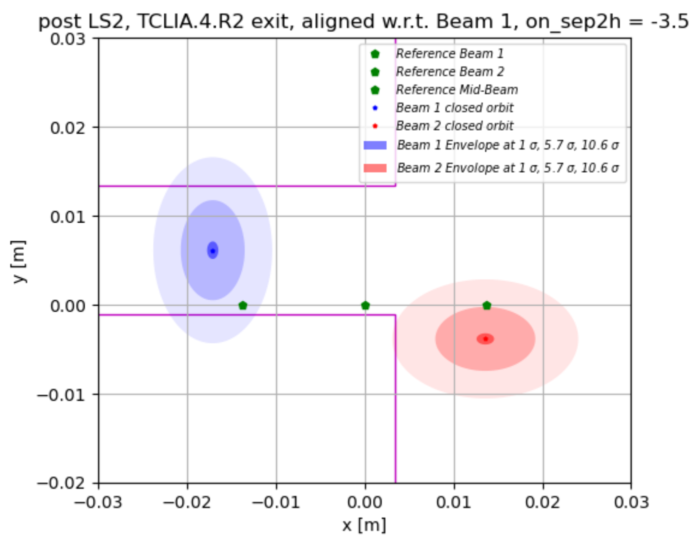

Figure 2.25: Post LS2, TCLIA exit, still incorrectly aligned. Here, the separation sign (on_sep2h) is inversed.

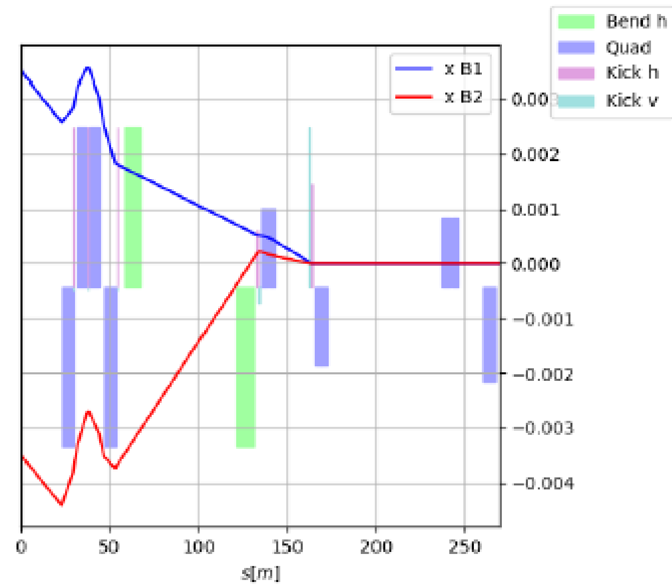

Figure 2.26: Beam orbit deviations with respect to the beam reference with the original separation sign

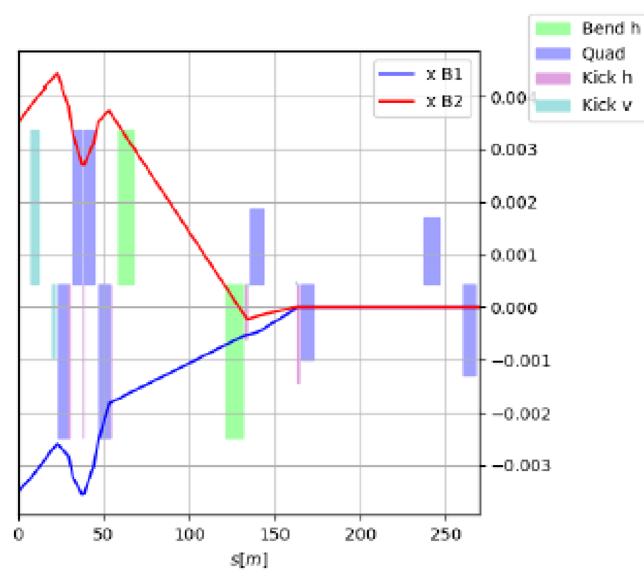

Figure 2.27: Beam orbit deviations with respect to the beam reference with an inverted separation sign.

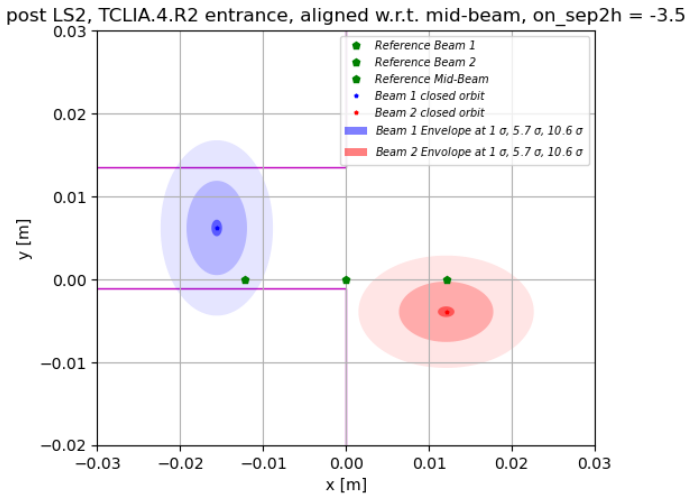

Figure 2.28: Post LS2, TCLIA entrance, correctly aligned for the completeness of the study. Here, the separation sign (on_sep2h) is inversed.

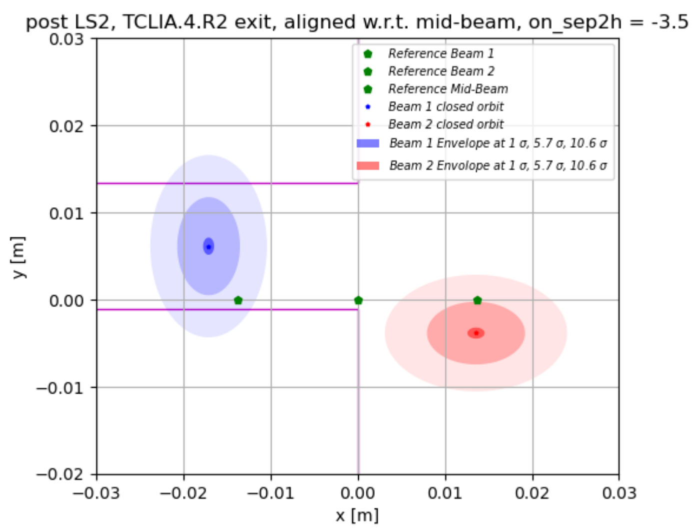

Figure 2.29: Post LS2, TCLIA exit, correctly aligned for the completeness of the study. Here, the separation sign (on_sep2h) is inversed.

2.2.5 Comments

The following problems arose during the present studies:

1. All the TCLIA have missing apertures in LDB, Figure 2.30
2. There are not sufficient drawings in EDMS that can fully describe the TCLIA
3. Some drawings are incorrect and not up-to-date, as an example the drawing [26] has an incorrect scale of 1:5, instead of the correct 1:4.

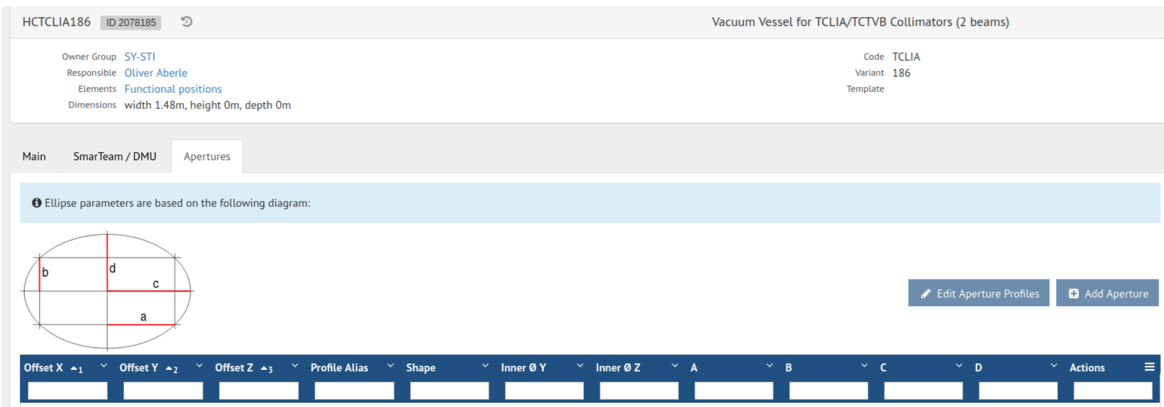

Figure 2.30: Aperture type for TCLIA is missing in LDB, [3] (now updated)

The constructed aperture, in Figure 2.31, was based on drawing [28]. The center of the aperture is $(U, V) = (0, 0)$.

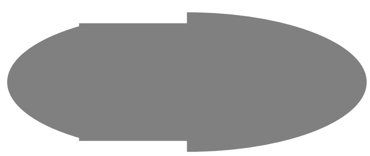

Figure 2.31: Aperture shape with the jaws opened in parking position (maximum) at $\pm 29mm$ [4]. Data gathered from drawing [28].

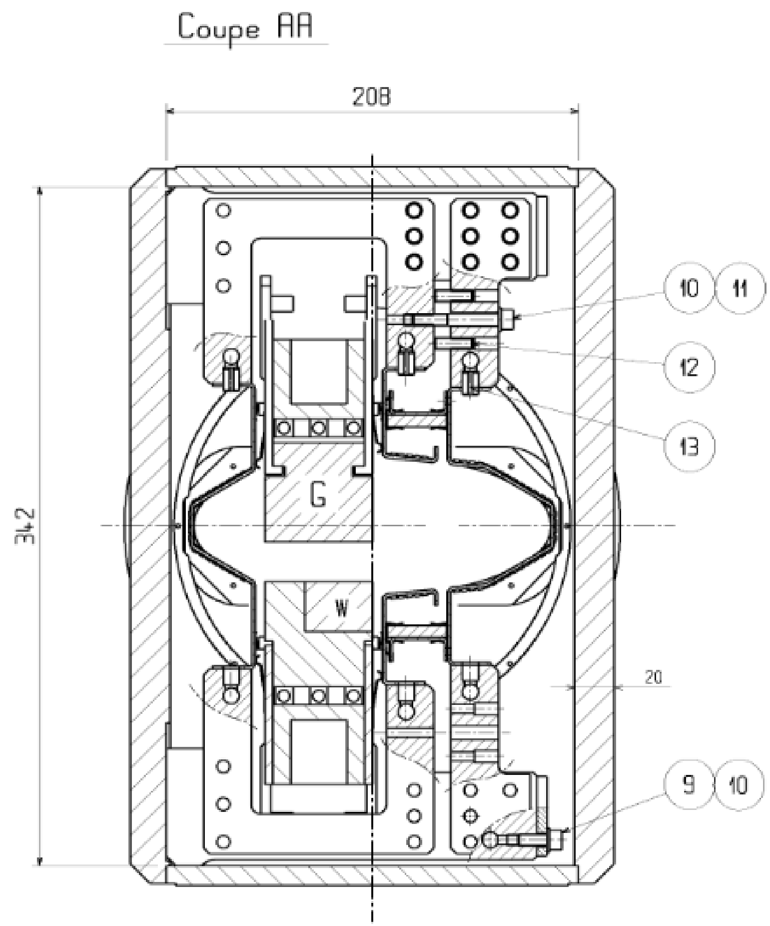

Figure 2.32: Apertures from drawings used to recreate the aperture in SVG. Picture from drawing [27].

2.2.6 Corrective measures

The proposed solutions to mitigate the problem are summarized in [21]. Very briefly: as the re-alignment of the TCLIA during the 2022-2023 YETS was thus excluded

Regarding the post LS3 period:

1. Keep the same approach as for Run III with a reversed sign for p+ runs only, without realigning the TCLIA.
2. Positive separation for all beams and realign TCLIA ($\geq 3.3mm$ movement, for larger movements possibly there is a need to adjust the position of sector valve and support of vacuum chamber).

Based on the above, we can conclude the following:

1. Applied solution for 2022 run: move right jaw to -6 mm to avoid intercepting B2 [8].
2. In 2023, profiting from the restart of the commissioning period, the sign of the separation was inverted allowing to achieve a considerable margin (as shown in Tables 2.2, 2.3. This configuration proved to be completely loss-free when performing the lossmaps validation. The sign inversion when operating with ions is more complex due to the required increase of the current in the MCBX horizontal correctors. Seen the reduced intensity, the solution of retracting the lower jaw to -6 mm, while keeping the 2022 separation angle, will be applied during the ions' run. [8].
3. The realignment of the TCLIA will be done during the YETS 2024-2025 in combination with VSC activities for the RF modules consolidation. The separation scheme used in 2023 should be considered as the baseline for the proton runs but, in case of major problems with the MCBX horizontal correctors (which show signs of degradation in IP1 and IP5), the possibility of reverting the separation sign has to be taken into account. [8].

2.2.7 Aperture insertion in LDB

Based on the measured aperture from the TCLIA drawings, as well as the corresponding aperture in SVG in File 2.31, the TCLIA aperture was inserted in LDB. The aperture had to be approximated by the ellipse $\frac{x^2}{90^2} + \frac{y^2}{35^2} = 1$ and a new aperture type, APTCLIA001, was introduced. The SVG image containing the aperture (that also points to the ACC models optics repository) was also added as a note.

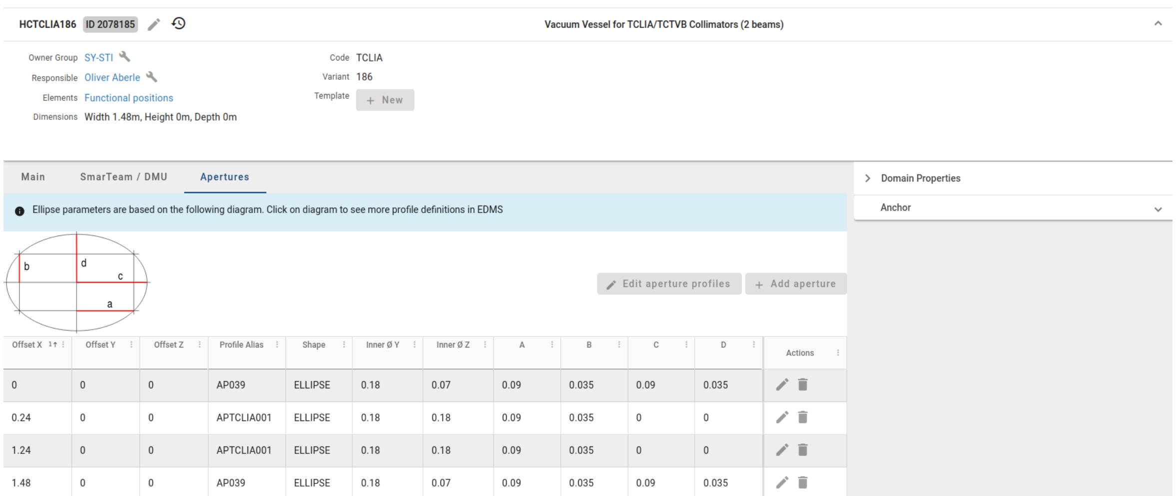

Figure 2.33: HTCLIA186 aperture inserted in LDB [3]

2.3 Superconducting RF Cavities at IP4

2.3.1 Overview

Because of the apertures missing for the Superconducting RF cavities at IP4, among other issues, there was an effort to review the data available in LDB, EDMS and drawings. The full document is available in EDMS [20]. The below brief description will focus on the data useful for beam studies and MAD-X simulations. Finally, the apertures of the RF cavities and the surrounding area will be defined, to the allowed by the gathered data precision. It is highlighted that the drawings checked were created more than 15 years ago, and no changes to the basic level were made in these years of LHC operation.

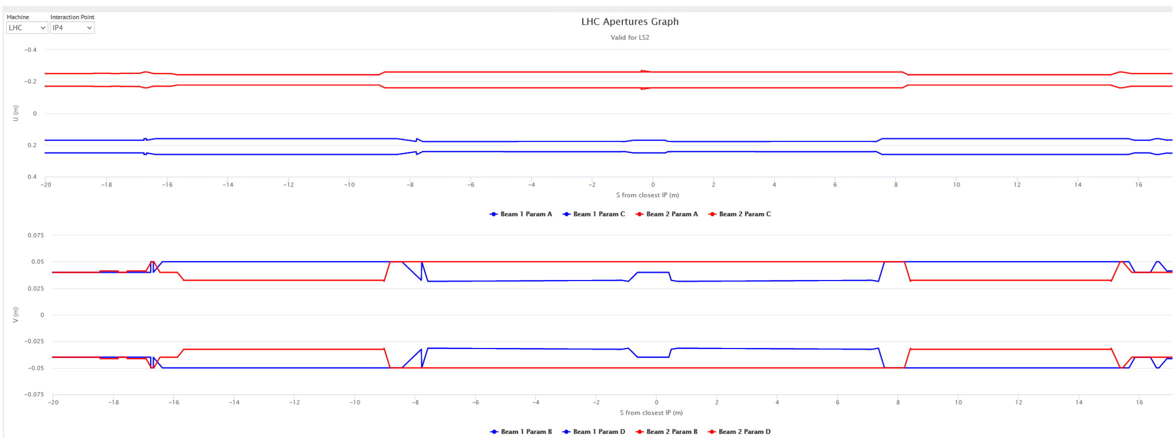

Figure 2.34: Aperture graph around IP4, where the Superconducting RF Cavities are installed. One cannot even notice that RF cavities are installed at this location.

The Superconducting RF Cavities are installed in sets of four, as they need to be in a cryogenic module. Each beam passes through a separate module when accelerated. The beam that is not accelerated passes through a bypass. Two modules are dedicated to accelerating Beam 1, and another two to accelerating Beam 2. This layout is shown in Figure 2.38. In Figure 2.35 there is the side view of the module, while in 2.37 the top view and the cross-section are depicted.

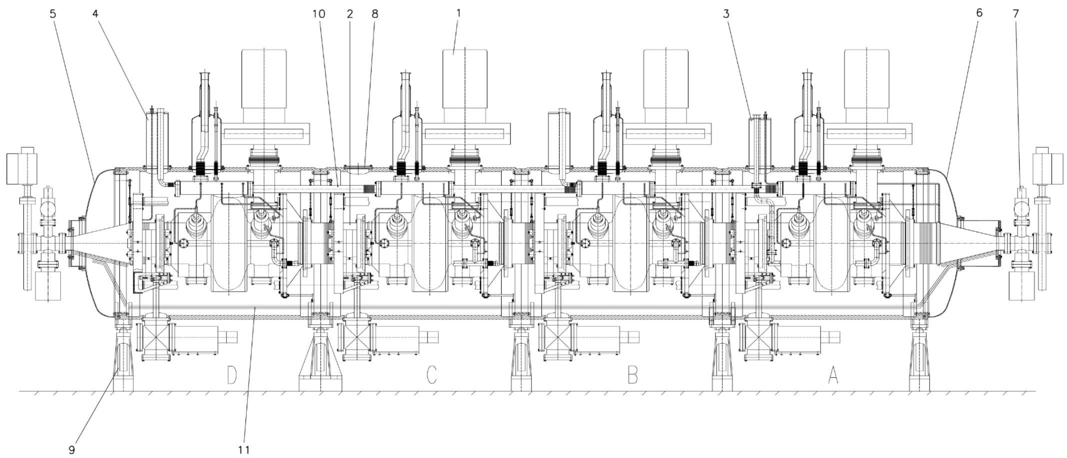

Figure 2.35: Side view of one module including 4 superconducting RF cavities [16]

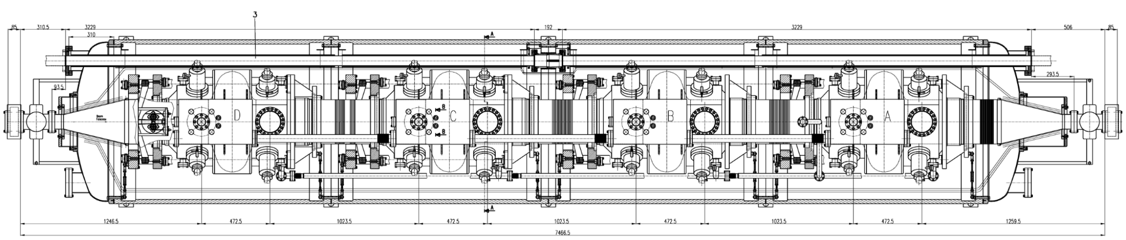

Figure 2.36: Top view of the module [17]

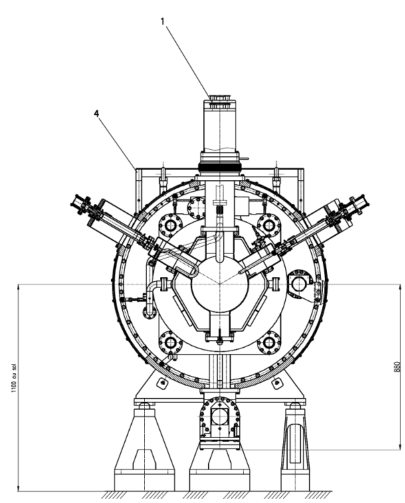

Figure 2.37: Front (cross-section) view of the module [17]

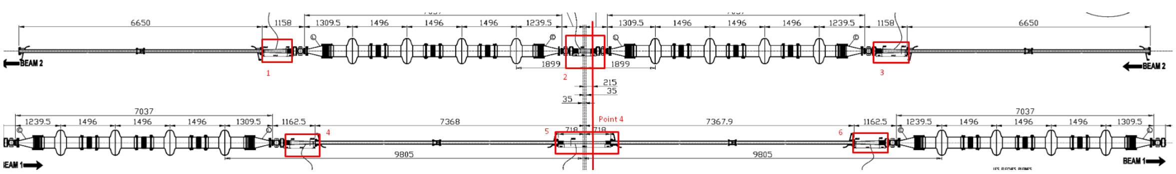

Figure 2.38: Layout around IP4, for Beam 2 (top) the modules are next to each other, when between them is IP4. For Beam 1 (bottom), the two modules are further separated [6]

2.3.2 Issues in LDB and drawings

Overall, the dimensions described in the drawings are consistent with the data inserted in LDB. Nonetheless, the drawings themselves are not in agreement with each other, even in key information such as the length of the accelerating part of the cavity. After internal communications with engineers from ACE and SY-RF, it was decided that the drawings are not reliable anymore and should ideally be updated to the current situation. As a result, a more reasonable approach is to compare the (although) simplified 3D drawings of the area, with of the ACE, and the corresponding data in the vacuum editor in LDB.

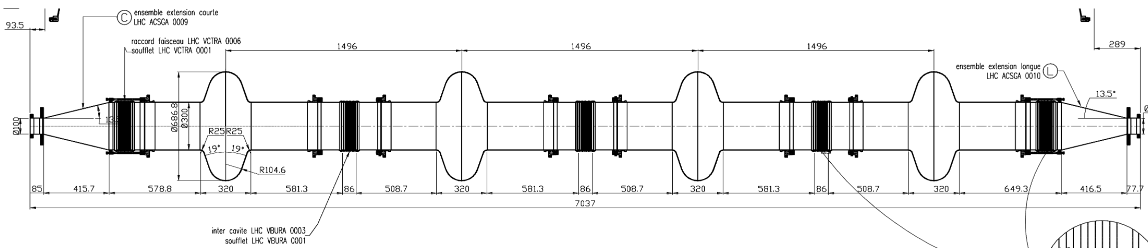

Figure 2.39: From drawing [6]

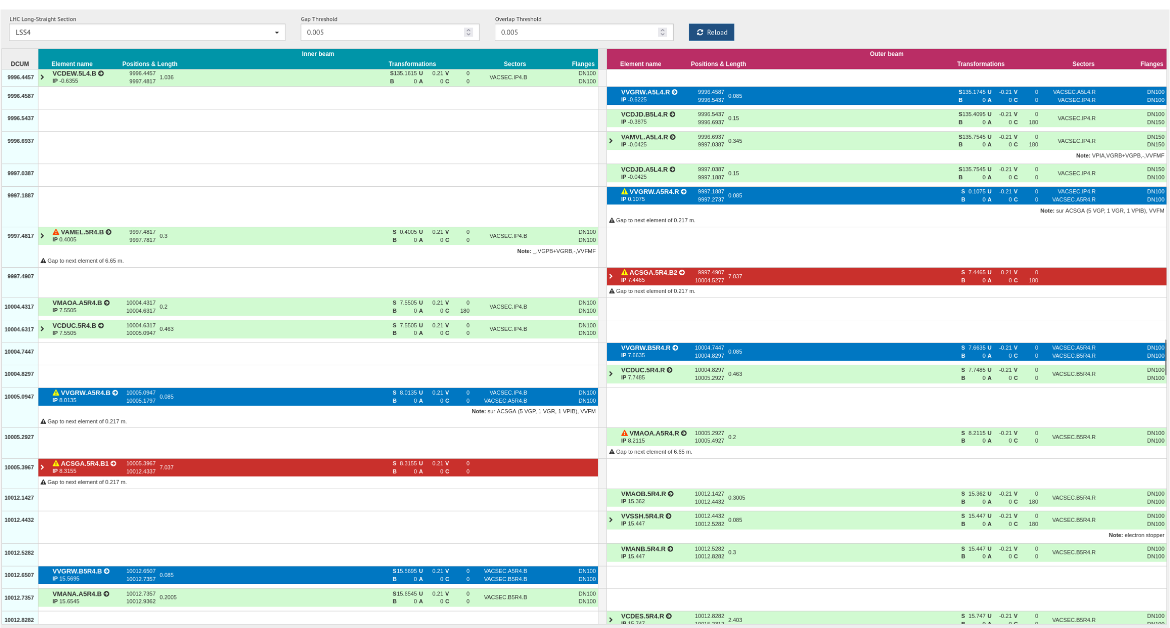

Figure 2.40: LHC Beam Vacuum Editor layout around ACSGA.5R4.B1 and ACSGA.5R4.B2

As a result, a more reasonable approach is to compare the (although) simplified 3D drawings of the area, with the help of the ACE group, and the corresponding data in the vacuum editor in LDB. Based on these comparisons, several missing elements on LDB were discovered, as well as others that have wrong or missing apertures. A full description can be found in [20].

Next, it should be noted that it is not clear or anywhere stated whether the drawing is representing the module in cold or warm conditions. Ideally, for the superconducting elements, both of the dimensions should be present in the LDB.

Regarding the fixed points, they are not described in the drawings, and they were found only in a CATIA drawing of the SR cavities. Based on this, the fixed points do not seem to be far from the central cross-section of the cavity, hence the distance between the two is very small. This distance is negligible for beam and optics studies since the maximum diameter of the cavity is 300 mm and the thermal contraction is around 300μm per meter.

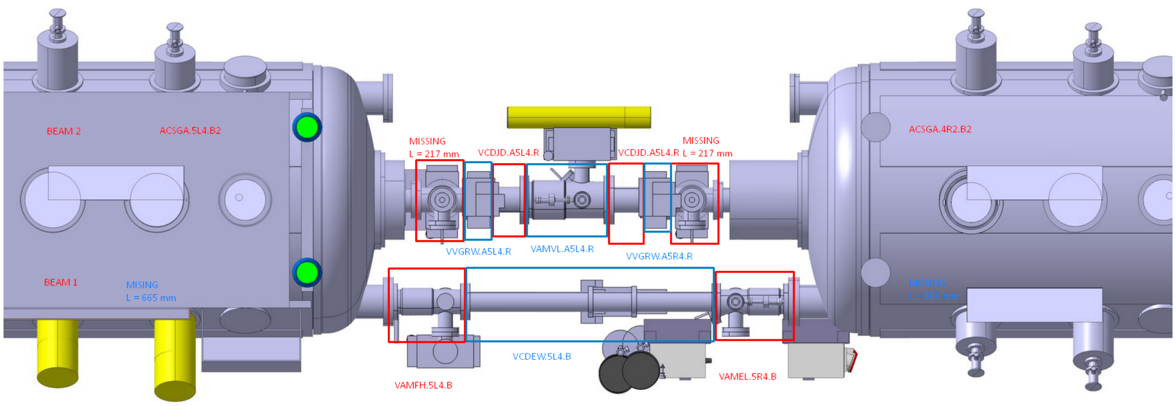

Figure 2.41: Layout between ACSGA.5L4.B2 and ACSGA.4R2.B2

2.3.3 Aperture definition

Despite the issues, we can still define the apertures on the cavities themselves and the surrounding area inside the cryomodule, as the aperture change they pose is significant. For defining the apertures for the superconducting cavities and the placeholders we need the circular apertures of 300mm [33], then the one of 686.8mm [34] and again the one of 300mm. The aperture changes of the whole cryomodule that hosts the cavities are shown in Figure 2.42.

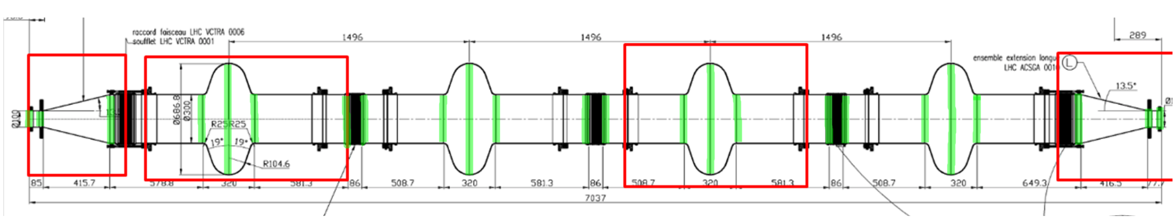

Figure 2.42: The red rectangles indicate the shapes of the cavities and the short cones. The green lines indicate the places where aperture shapes will be inserted in LDB. [6]

All the below apertures are based on [6].

For the ease of inserting the apertures on LDB, Table 2.5 is created with all the apertures at

Name	Type	C rotation
ACSGA.5L4.B1	HCACSGA001	0
ACSGA.5L4.B2	HCACSGA001	180
ACSGA.5R4.B2	HCACSGA002	180
ACSGA.5R4.B1	HCACSGA002	0

Table 2.4: Type and orientation of the cavities.

distinct points of the module. The slices where the aperture is inserted are indicated with green lines in Figure 2.42. The apertures are inserted at the level of the top assembly.

Note: C rotation is a clockwise rotation around the vertical axis V.

comments	offset X	offset Y	offset Z	Profile Alias	shape	Inner Y diameter	Inner Z diameter	A	B	C	D
transition chamber 1	0	0	0	AP010	CIRCLE	0.1	0.1	0.05	0.05	0.05	0.05
transition chamber 1	0.085	0	0	AP010	CIRCLE	0.1	0.1	0.05	0.05	0.05	0.05
transition chamber 1	0.5007	0	0	AP0430	CIRCLE	0.3	0.3	0.15	0.15	0.15	0.15
cavity placeholder	1.0795	0	0	AP0430	CIRCLE	0.3	0.3	0.15	0.15	0.15	0.15
cavity	1.1612	0	0	ND	CIRCLE	0.60732	0.60732	0.30366	0.30366	0.30366	0.30366
cavity	1.2395	0	0	AP0431	CIRCLE	0.6868	0.6868	0.3434	0.3434	0.3434	0.3434
cavity	1.3212	0	0	ND	CIRCLE	0.60732	0.60732	0.30366	0.30366	0.30366	0.30366
cavity placeholder	1.3995	0	0	AP0430	CIRCLE	0.3	0.3	0.15	0.15	0.15	0.15
binding	1.9808	0	0	AP0430	CIRCLE	0.3	0.3	0.15	0.15	0.15	0.15
binding	2.0668	0	0	AP0430	CIRCLE	0.3	0.3	0.15	0.15	0.15	0.15
cavity placeholder	2.5755	0	0	AP0430	CIRCLE	0.3	0.3	0.15	0.15	0.15	0.15
cavity	2.6572	0	0	ND	CIRCLE	0.60732	0.60732	0.30366	0.30366	0.30366	0.30366
cavity	2.7355	0	0	AP0431	CIRCLE	0.6868	0.6868	0.3434	0.3434	0.3434	0.3434
cavity	2.8172	0	0	ND	CIRCLE	0.60732	0.60732	0.30366	0.30366	0.30366	0.30366
cavity placeholder	2.8955	0	0	AP0430	CIRCLE	0.3	0.3	0.15	0.15	0.15	0.15
binding	3.4768	0	0	AP0430	CIRCLE	0.3	0.3	0.15	0.15	0.15	0.15
binding	3.5628	0	0	AP0430	CIRCLE	0.3	0.3	0.15	0.15	0.15	0.15
cavity placeholder	4.0715	0	0	AP0430	CIRCLE	0.3	0.3	0.15	0.15	0.15	0.15
cavity	4.1532	0	0	ND	CIRCLE	0.60732	0.60732	0.30366	0.30366	0.30366	0.30366
cavity	4.2315	0	0	AP0431	CIRCLE	0.6868	0.6868	0.3434	0.3434	0.3434	0.3434
cavity	4.3132	0	0	ND	CIRCLE	0.60732	0.60732	0.30366	0.30366	0.30366	0.30366
cavity placeholder	4.3915	0	0	AP0430	CIRCLE	0.3	0.3	0.15	0.15	0.15	0.15
binding	4.9728	0	0	AP0430	CIRCLE	0.3	0.3	0.15	0.15	0.15	0.15
binding	5.0588	0	0	AP0430	CIRCLE	0.3	0.3	0.15	0.15	0.15	0.15
cavity placeholder	5.5675	0	0	AP0430	CIRCLE	0.3	0.3	0.15	0.15	0.15	0.15
cavity	5.6492	0	0	ND	CIRCLE	0.60732	0.60732	0.30366	0.30366	0.30366	0.30366
cavity	5.7275	0	0	AP0431	CIRCLE	0.6868	0.6868	0.3434	0.3434	0.3434	0.3434
cavity	5.8092	0	0	ND	CIRCLE	0.60732	0.60732	0.30366	0.30366	0.30366	0.30366
cavity placeholder	5.8875	0	0	AP0430	CIRCLE	0.3	0.3	0.15	0.15	0.15	0.15
transition chamber 2	6.5368	0	0	AP0430	CIRCLE	0.3	0.3	0.15	0.15	0.15	0.15
transition chamber 2	6.9533	0	0	AP010	CIRCLE	0.1	0.1	0.05	0.05	0.05	0.05
transition chamber 2	7.031	0	0	AP010	CIRCLE	0.1	0.1	0.05	0.05	0.05	0.05

Table 2.5: Apertures of the Superconducting cavities' module

Chapter 3
Different models

Aperture models are one of the key elements of an optics model, together with the layout and strengths of the magnets. Aperture information is needed to design, validate, and operate the machine optics because they allow to determine:

- whether a device (element) can be installed
- whether the beam can be injected
- the minimum β^* (the β-function at the interaction point) for the experiments, to figure out the performance and the amount of luminosity that we will get
- the gap of the collimators
- the beam losses in the machine as well as their exact location

To date, there are three main and independent repositories in different levels of detail:

1. The first one is maintained by the ABP optics team, and it is relatively coarse. It is mostly used for designing and contains the aperture of the main magnetic elements, but not the vacuum transitions for instance. Used only for optics-related types of studies.
2. The second is maintained by the ABP collimation team. This one is more detailed, and it has to be continuous. It is used to determine the losses around the machine.
3. The third is maintained by EN-ACE (delegated to TE-VSC for LHC) in LDB. This one is the most detailed, but it has only been used for offline checks, and not systematically.

Since 2018, there has been an effort, started by Riccardo De Maria, to use the LDB for systematic studies in the LHC, as the data available there are the most detailed. The goal is to have a single source of truth for the apertures. Having three models, it is difficult to know which one is right, and which one is up-to-date. In addition, it is important to share the same data with the engineering teams, which should be the source of the aperture. Having an aperture model in LDB also gives the opportunity to locate mechanical features in the layout, without having to go through the mechanical drawings (which is already a very time-consuming task). The mechanical drawings often do not have enough reference points, so it is easy to relate the data in LDB with the mechanical instrument at the installed location.

When talking about the aperture model, the following should be stated:

- the vacuum aperture profiles defined by shapes that define cross-sections, the offset (TS, TU, TV) to specify where these cross-section are. Therefore, we need the longitudinal and transverse position, and roll (RS), which is the tilt with respect to the longitudinal axis.
- a simple shape can be a: circle, ellipse, rectangle, rectellipse, racetrack, octagon (in the Figure 3.1 there is a list of shapes that are currently supported by MAD-X and LDB. There are at most 4 parameters, and their meaning is specific to the shape. The idea behind choosing these parameters is to make sure A and B somehow reflect the horizontal and vertical gap. It is one choice out of all the other possible.

Lately, it became clear that we also need a generic shape. Some evident examples are the TCLIA and the TDIS, which were discussed in detail previously. For this generic shape, the proposed solution is the SVG Path, which is a widely used W3C standard (e.g. ”M x1 y1 x2 y2” is a valid SVG Path). Another solution could be to approximate apertures with polygons. Polygons are the most straightforward way to express a shape, but in the most common aperture shapes in the LHC, we would need a lot of shapes to get a good approximation. An SVG path is a way to encode a 2D shape, a strange aperture, such as the TDIS with the jaws on. And then you model any shape. The SVG path defines a path to a string of coordinates. This format is understood by any browser, and many libraries. The proposed editor is very easy to use, free, with a few commands only, and the link contains all the information for the path. It is a very flexible way to define apertures.

Starting with a bit of history, back in 2018 it was noted that the aperture data in LDB for the LHC had flaws, and a simple aperture viewer was used to illustrate the issues and the discrepancies. The aperture graphs became available in 2019 in LDB for the LHC and a few months later for the SPS, by Pascal Le Roux. Since then, it has been extremely useful to debug apertures and to resolve major issues in the LHC and SPS. For example, the exchange of aperture between the two beams or to see a natural description of the beam pipe.

Nonetheless, the present aperture viewer is not sufficient to help in understanding smaller inconsistencies and possibly their sources.

An improvement of the viewer in LDB would be expensive and therefore we have decided to develop a new approach in Python, thanks to the direct SQL views provided by Pascal. The new approach allows seeing tiny details, and the gaps of aperture. To do this in LDB takes a lot of time, and by the way the apertures are plotted, it is easier to find the source of the problem.

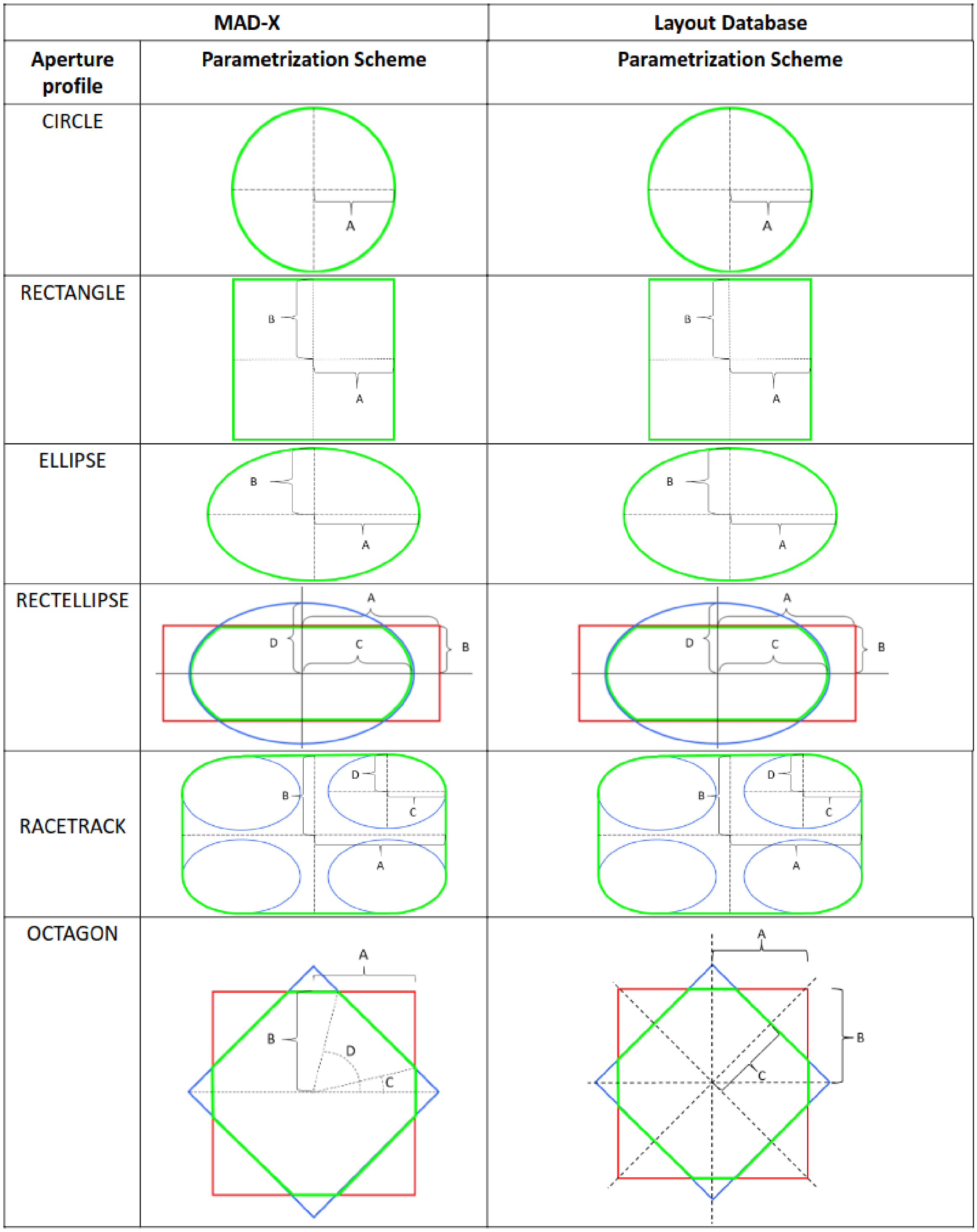

Figure 3.1: Different types of aperture profiles and their parametrization in MAD-X and LDB, [25]

Chapter 4
PyLayout

The project is implemented in a Python library and it is available on: `https://gitlab.cern.ch/layout/pylayout`. The library can be installed either locally or on SWAN. The installation guide is available in the README file in GitLab.

4.1 Different modules

We can start by making an overview of the functionalities of the different modules included.

Starting with `table.py` module is the starting point of the Python package, focusing on the management and manipulation of table-like data structures. This module provides a connection to the database and interaction with it. It retrieves column names from a specified table, counts the number of rows, and fetches all table names. Additionally, it can execute queries to obtain specific data views, such as element profiles filtered by shape, alias, or type, and apertures filtered by element name, shape, or alias, providing flexibility for detailed data retrieval. Furthermore, the class includes methods to convert SQL query results into pandas DataFrames facilitating data analysis. This module is crucial for dynamically managing and analyzing large sets of layout-related data within the package.

The `elements.py` module focuses on the definition, manipulation, and analysis of elements. It also defines a dictionary `machine_id` that maps machine names to their respective IDs, facilitating the identification and processing of machine-specific data.

Central to the module is the Elements class, which manages a collection of element objects. This class provides methods to create elements from a table of data, filter them based on specific patterns, and analyze their properties.

Complementing the Elements class is the Sequence class, which represents a sequence of nodes and provides methods to manipulate and analyze these sequences. These classes encapsulate individual elements, capturing detailed positional and transformation data, and providing a powerful tool for managing and analyzing the geometric and spatial properties of elements.

The `tablemixin.py` module enhances table-like data structures with advanced functionalities such as flexible indexing, filtering, expression evaluation, and pretty printing. Next, the `canvas.py` module is useful for visualizing and manipulating geometric entities within the package. It provides classes for defining points, lines, curves, arcs, and text, and includes comprehensive 2D and 3D canvases for rendering these primitives. These utilities overall facilitate graphical representation. The `curvelib.py` module is designed for the creation and manipulation of curve segments based on various specifications. This module defines a flexible framework for generating, rendering, and analyzing curves. The last two modules, although mentioned for completeness, will not be used in the later plots, as their functionalities are designed for a later version of the library.

The `svgutils.py` module is used for handling SVG data. It processes the SVG path commands, extracting coordinate data and transforming it into a structured list of points. This conversion is crucial for integrating SVG-defined shapes into geometric computations and visualizations within the package.

Finally, `madutils.py` module provides the final horizontal and vertical plots, and it is the core of the library. Its main purpose is to make sense of the data provided for each element in order to plot them correctly. This module also facilitates the integration of MAD-X data into the package's framework, enabling visualization of the beams and their envelopes on the same plot as the aperture.

These last modules will be discussed in more detail in the following sections.

4.2 Outputs

First, it is important to define how a single element is plotted. Taking as an example the very first element in the LHC sequence (in Figure 4.1): `([('VC1AX.1R1.X', [(4.54, 'HCVC1AX', 'IE', 'CIRCLE', (0.029, 0.029, 0.029, 0.029), 0.0, 0.0, 0.0), (9.0, 'HCVC1AX', 'IE', 'CIRCLE', (0.029, 0.029, 0.029, 0.029), 0.0, 0.0, 0.0)]), ('VC1TB.1R1.X', [(9.0, 'HCVC1TB', 'IE', 'CIRCLE', (0.029, 0.029, 0.029, 0.029), 0.0, 0.0, 0.0)])])` this is a dictionary with the name of the element as well as some markers at distinct s locations on it. 'HCVC1AX' is the aperture profile type, 'IE' indicates that it hosts both beams, 'CIRCLE' denotes the shape of the aperture, (0.029, 0.029, 0.029, 0.029) are the aperture parameters (ABCD), and last, there are the three angles, theta, phi, psi.

The way an element is plotted is by taking the locations (s coordinate) of each marker in a single element and applying the aperture offsets on it, horizontally or vertically. This is done in a way that the final shape is closed, in the sense that we start from the bottom left side of the element, and circle around the element until we reach again the starting point. This approach enables to fully describe the geometry of the element and helps to reveal potential issues. In the end, each element is represented by a set of coordinates that define the boundary of the aperture (like a polygon) and they are always closed, meaning that the first and last coordinates are the same. This facilitates the plotting of the aperture later on. Example: (name, [x1, x2, x3, x4, x1]): [('VC1AX.1R1.X', [4.54, 9.0, 9.0, 4.54, 4.54])] representing the longitudinal offsets and (name, [y1, y2, y3, y4, y1]): [('VC1AX.1R1.X', [0.029, 0.029, -0.029, -0.029, 0.029]) representing the transverse offsets.

For the vertical plots, the two beams are plotted separately, as otherwise, they would overlap. The library provides many functionalities, that are asked from the user to be given as arguments.

- start: The starting point of the range to plot (default: 0).
- end: The ending point of the range to plot (default: 28000).
- machine: The name of the machine (default: "LHC").
- version: The version of the machine (default: "EYETS 2023-2024").

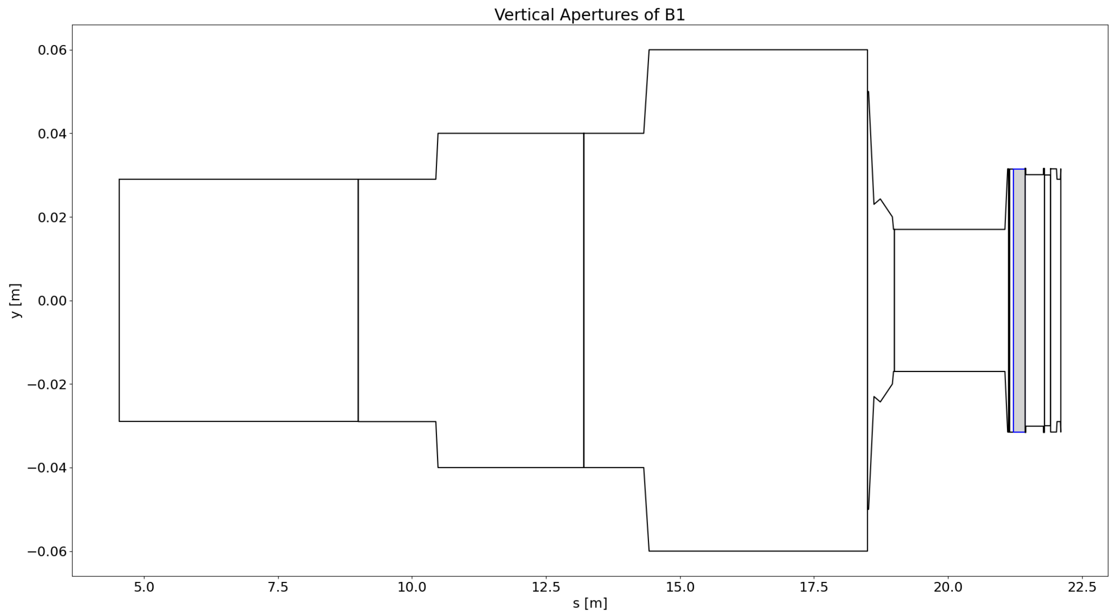

Figure 4.1: Apertures of the first elements in the LHC sequence

- label: Whether to label the apertures (default: False).
- madx: Whether to use MAD-X for plotting (default: True).
- find_gaps: Whether to find aperture gaps (default: False).
- tolerance: The tolerance for finding gaps (default: 0.002).
- which_beam : The beam to plot apertures for (”b1” or ”b2”) (default: ”b1”).

In that way, we can get a plot of the vertical apertures in the requested range, in the requested machine, and with the data coming from a specific version of the LDB. There is the possibility of finding gaps in apertures, as at some points elements are missing in the database. In this case, the user can specify the minimum distance considered as a gap (tolerance). In the case there are gaps, a DataFrame containing information about them, including the gap distance, the name of the first element, the maximum s-coordinate of the first element, the name of the second element, and the minimum s-coordinate of the second element is printed. In addition, if there are any overlapping elements, the left one is plotted with blue boundaries, and filled in gray color.

We can plot the entire layout of the LHC, as seen in Figure 4.2 in a straight line. Of course, to see the apertures and the layout we have to zoom in.

In another example, Figure 4.3 we can plot the vertical apertures around IP5. It is noted that we are mostly interested about the layout around the IPs, roughly ($\pm 200m$) around an IP, as these are the regions that undergo frequent changes. The layouts of the arcs remain the same and hardly ever present any issues in terms of apertures and layout. In Figure 4.4, we also see the names of the elements. In this case, as we are plotting a long-range, some labels land on top of each other, as they are installed in close to one another.

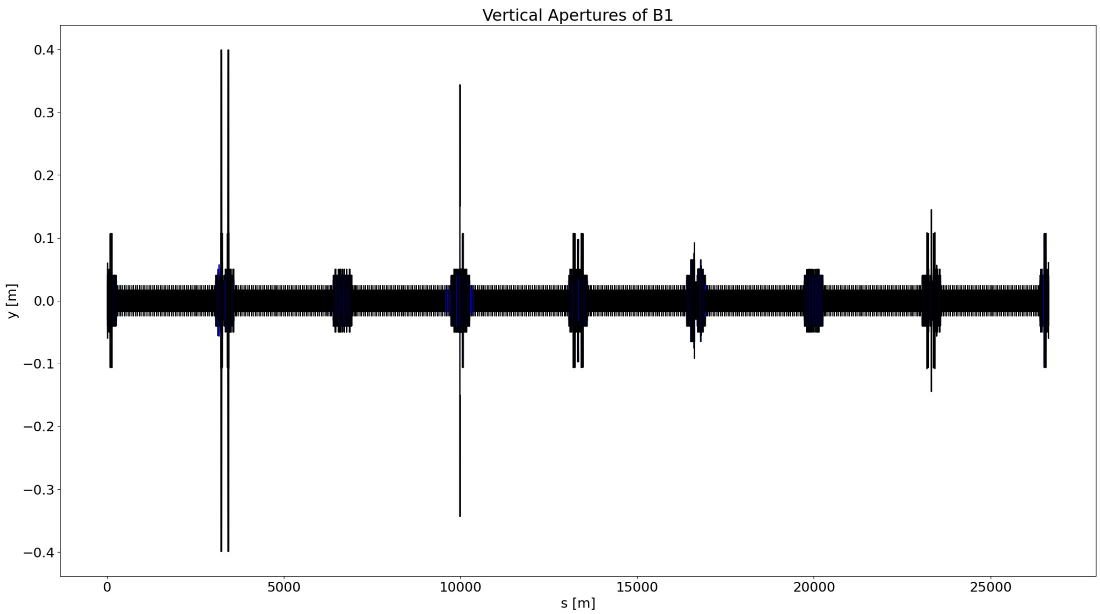

Figure 4.2: Vertical apertures of B1 and layout of the whole LHC.

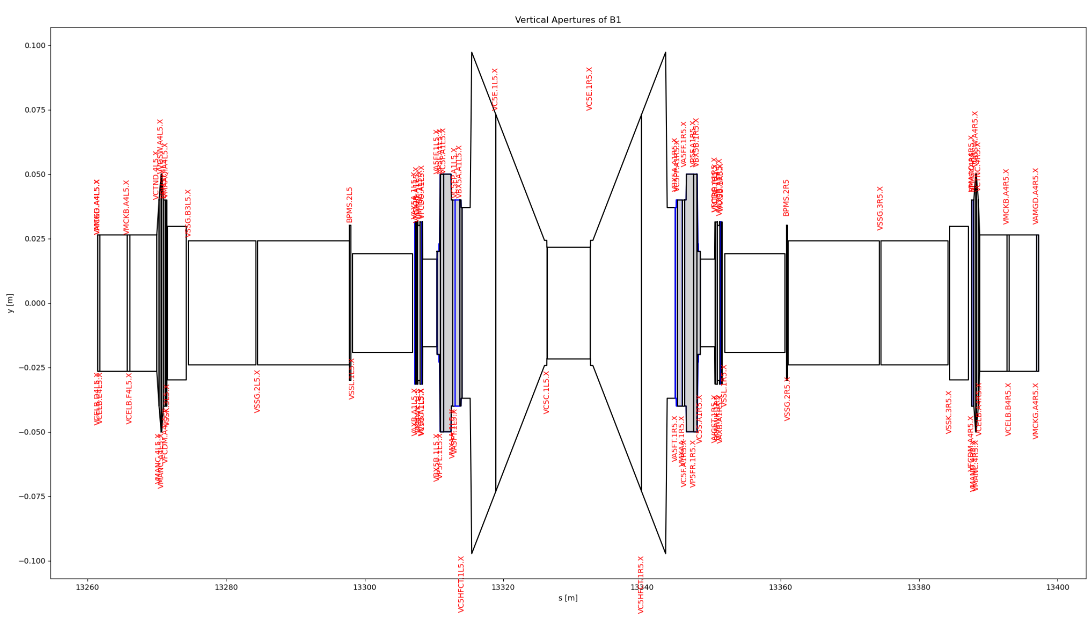

Figure 4.3: Vertical apertures of B1 and layout around IP5, with visible labels of the elements

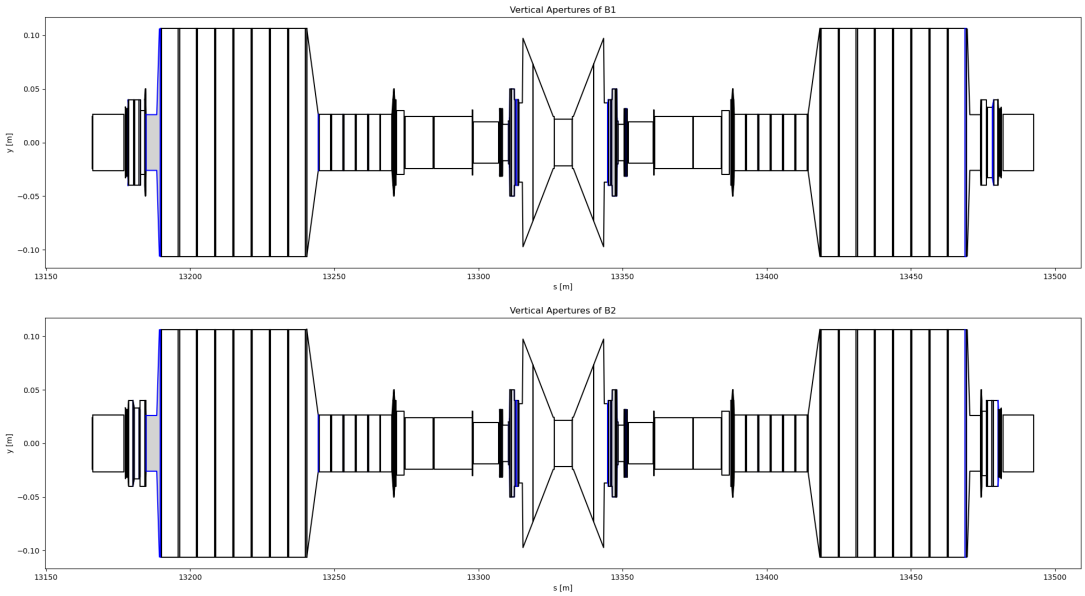

Figure 4.4: Vertical apertures and layout around IP5, the two beams are plotted separately. There are no differences in the plots, as the beams are hosted in the same pipe.

Next, in Figure 4.4, we see both of the beams in parallel. In this example, there are no differences, as the beams are hosted in the same pipe anyway. In this figure, as well as the previous one, we can see some elements overlapping, as they are highlighted in blue, and filled with gray. This suggests that the longitudinal coordinate might have been inserted incorrectly in LDB. These kinds of issues are not easy to spot in LDB, as the person inserting the data cannot see the change in the layout.

In figure 4.5, the vertical apertures of both beams are plotted to start a bit before IP2. On the right side, the arc begins, showing the repetitive layout of the FODO cells. These areas are also symmetrical for both beams, thus it is normal for the plots to look very similar. Nonetheless, the two beams have to be plotted separately.

Next, we can continue with the horizontal apertures, i.e. the beams seen from the top. Here, the two beam pipes are always depicted in the same plots, as they never coincide. In Figure 4.6, the horizontal apertures around IP5 are plotted. The convergence of the beams when approaching the IP is visible, as well as the separation after the IP. This is always the case in the IPs.

In the case of horizontal apertures, I (internal), E (external), and IE (internal/external) markers should be plotted separately, to avoid confusion between the boundaries of the elements. In the case that a single element has both of these types, the crossing aperture lines are removed entirely.

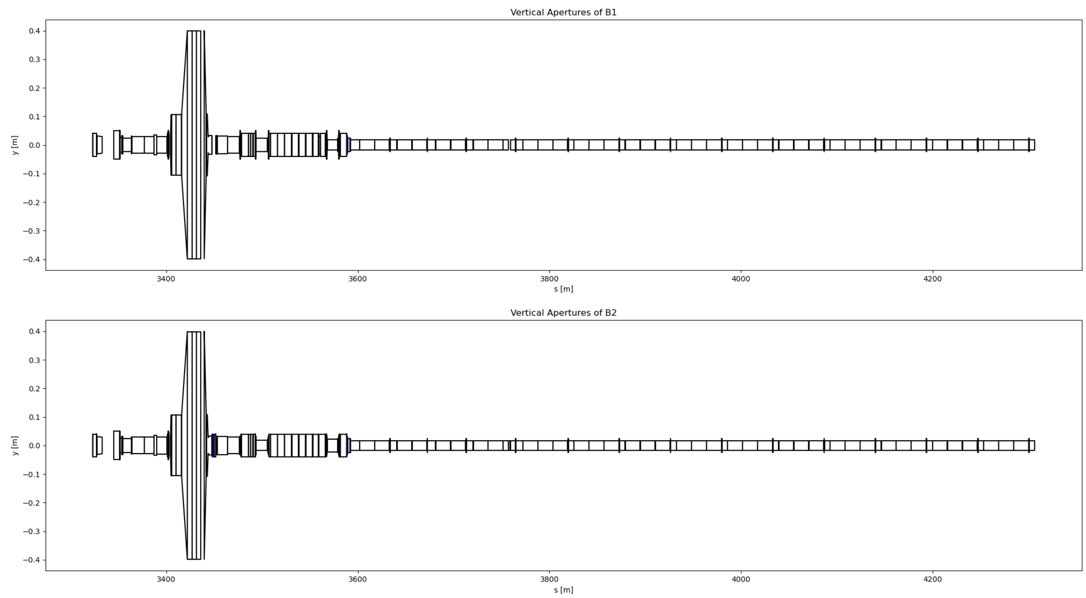

Figure 4.5: Vertical apertures and layout, IP2, the two beams are plotted separately. On the right side, we can see the beginning of the arcs

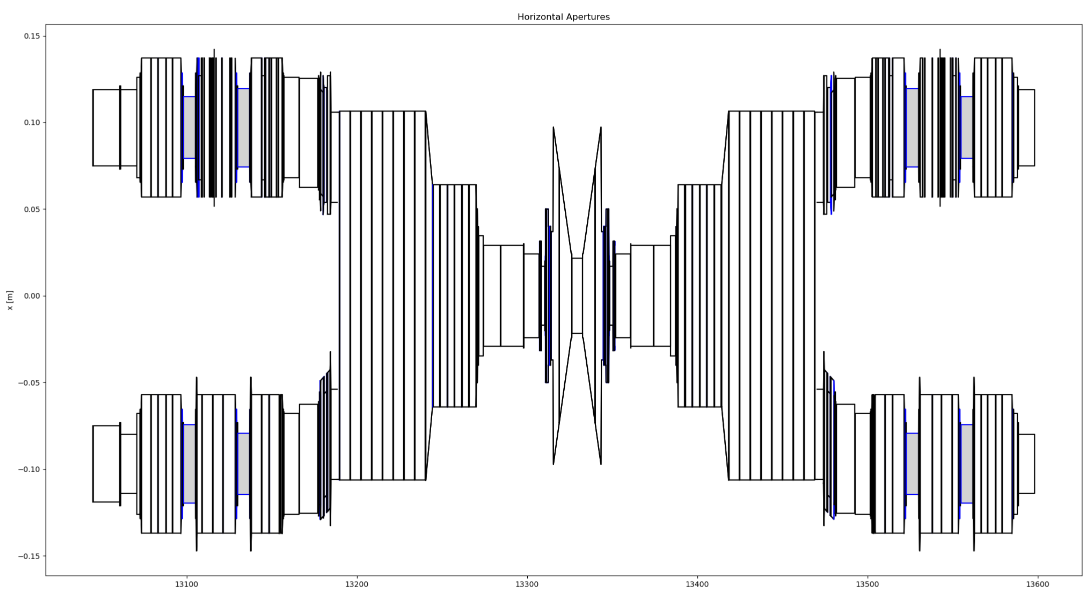

Figure 4.6: Horizontal apertures and layout around IP5

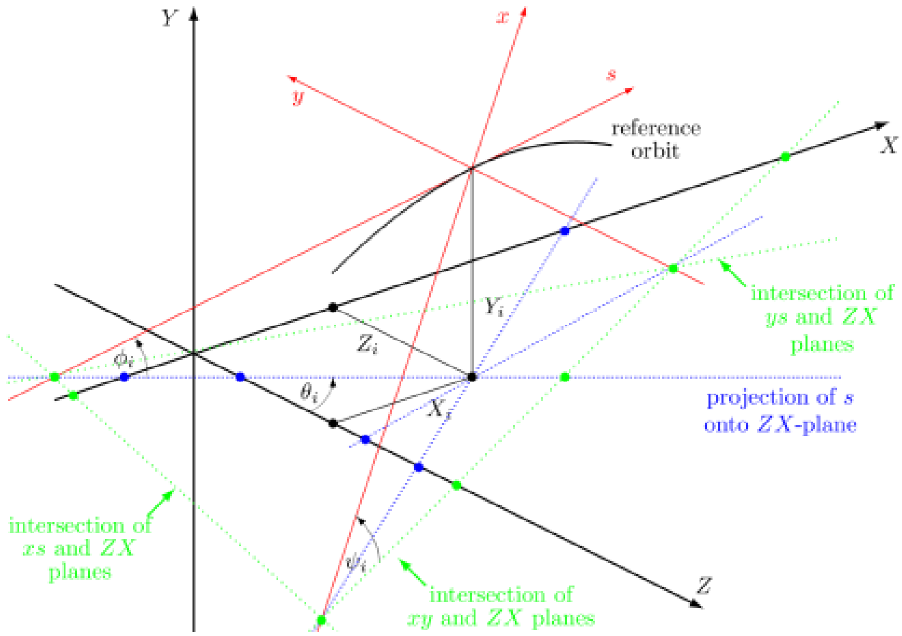

Figure 4.7: "Global Reference System showing the global Cartesian system (X, Y, Z) in black and the local reference system (x, y, s) in red after translation (X_i, Y_i, Z_i) and rotation (θ_i, φ_i, ψ_i). The projections of the local reference system axes onto the horizontal ZX plane of the Cartesian system are shown with blue dashed lines. The intersections of planes ys, xy, and xs of the local reference system with the horizontal ZX plane of the Cartesian system are shown in green dashed lines" as described in the MAD-X manual [12]

4.3 Plots with beam

4.3.1 Transformation from local to global coordinate system

As discussed in the introduction, due to various errors like misalignment errors, field errors, and so on, the closed orbit does not exactly line up with the reference orbit. The closed orbit also changes with the momentum errors. The closed orbit is described with respect to the reference orbit, using the local reference system (X, Y, S).

The global reference orbit is uniquely defined by the sequence of the physical elements. The local reference system (X, Y, S) may be referred to as a global Cartesian coordinate system (X, Y, Z).

The local reference system (x_i, y_i, s_i) at position i, i.e. the displacement and direction of the reference orbit with respect to the global Cartesian coordinate system are defined by three displacements (X_i, Y_i, Z_i) and three angles (θ_i, φ_i, ψ_i).

We can define the following (this definition is directly taken from the MAD-X manual):

- θ: The angle of rotation (azimuth) about the global Y-axis, between the global Z-axis and the projection of the reference orbit onto the (Z, X)-plane. A positive angle θ forms a right-hand screw with the Y-axis.

- φ: The elevation angle, i.e., the angle between the reference orbit and its projection onto the (Z, X)-plane. A positive angle φ corresponds to increasing Y.

- ψ: The roll angle about the local s-axis, i.e., the angle between the line defined by the intersection of the (x, y)-plane and (Z, X)-plane on one hand, and the local x-axis on the other hand. A positive angle ψ forms a right-hand screw with the s-axis.

- The angles (θ, φ, ψ) are not the Euler angles. The reference orbit starts at the origin and points by default in the direction of the positive Z-axis.

We can define the following transformation matrices, where θ, ψ, φ are the angles taken from the survey module in MAD-X. These definitions can also be found in more detail in the MAD-X manual in [12].

$$\Theta = \begin{bmatrix} \cos(\theta) & 0 & \sin(\theta) \\ 0 & 1 & 0 \\ -\sin(\theta) & 0 & \cos(\theta) \end{bmatrix},$$

$$\Phi = \begin{bmatrix} 1 & 0 & 0 \\ 0 & \cos(\varphi) & \sin(\varphi) \\ 0 & -\sin(\varphi) & \cos(\varphi) \end{bmatrix},$$

$$\Psi = \begin{bmatrix} \cos(\psi) & \sin(\psi) & 0 \\ -\sin(\psi) & \cos(\psi) & 0 \\ 0 & 0 & 1 \end{bmatrix}.$$

For each point, the transformation matrix W is computed as:

$$W = [\Theta \quad \Phi \quad \Psi].$$

The unit vectors in the new coordinate system are:

$$e_x = W \begin{bmatrix} 1 \\ 0 \\ 0 \end{bmatrix}, \quad \text{and} \quad e_y = W \begin{bmatrix} 0 \\ 1 \\ 0 \end{bmatrix}.$$

The closed orbit coordinates for each point are then computed as:

$$\text{co} = \begin{bmatrix} su.x \\ su.y \\ su.z \end{bmatrix} + tw.x \times e_x + tw.y \times e_y,$$

where $su.x$, $su.y$, $su.z$ are computed by the SURVEY command, which gives the geometrical layout, which is the coordinates of all machine elements in a global reference system. These coordinates don't take into account the closed solution that MAD-X produces. For this reason, the computed coordinates in the local reference system produced by the twiss module should be considered, i.e. $tw.x$, $tw.y$, and therefore translated into the global reference system. After having translated the beams into the global reference system, they can be plotted in the aperture plots.

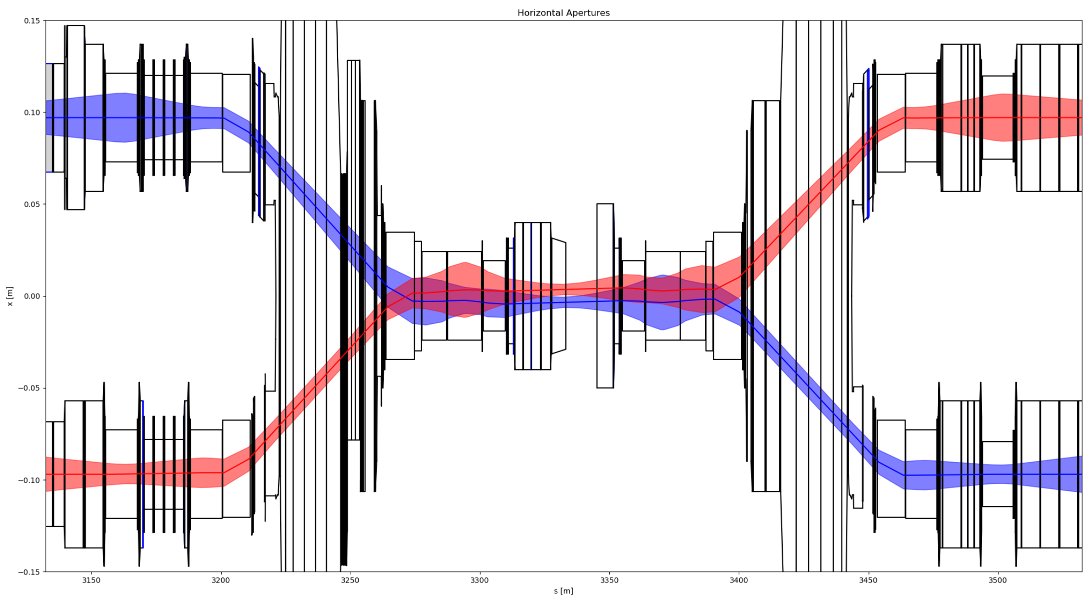

Figure 4.8: Horizontal apertures and layout around IP2, with Beams and beam sizes at 10.6 σ at injection energy

4.3.2 Plots

Thanks to the transformation matrices from local to global coordinates, it is possible to plot the beams inside the aperture and layout, around the IPS. These plots provide a realistic view of how the final situation will look like. This plot can have a beam envelope of different sigma, here is plotted at 10.6 σ, as we consider that after this point hardly any particles will be found. Indeed, after also plotting the beam, it is clear that the aperture margin in many cases drops by a lot, and in cases of misalignment, like the TCLIA, it would have been evident that the beam envelope touches the aperture boundaries. In the case of plotting the beams, one parameter that should be specified is the correct optics model in MAD-X. For the example below, `acc-models-lhc/scenarios/pp_lumi/RAMP-SQUEEZE-6.8TeV-ATS-2m-2023/_V1/0/model.madx` from the ACC models repository, `https://gitlab.cern.ch/acc-models/`. These models are maintained by the ABP and changed every year. They include many operational scenarios in all the different energies that the accelerators will run. In Figure 4.8, the horizontal apertures are depicted, and in Figure 4.9 the vertical ones. In Figure 4.9, also the reference beam (for each beam) from the survey is visible. For both beams, the reference beam always lays on the XY plane.

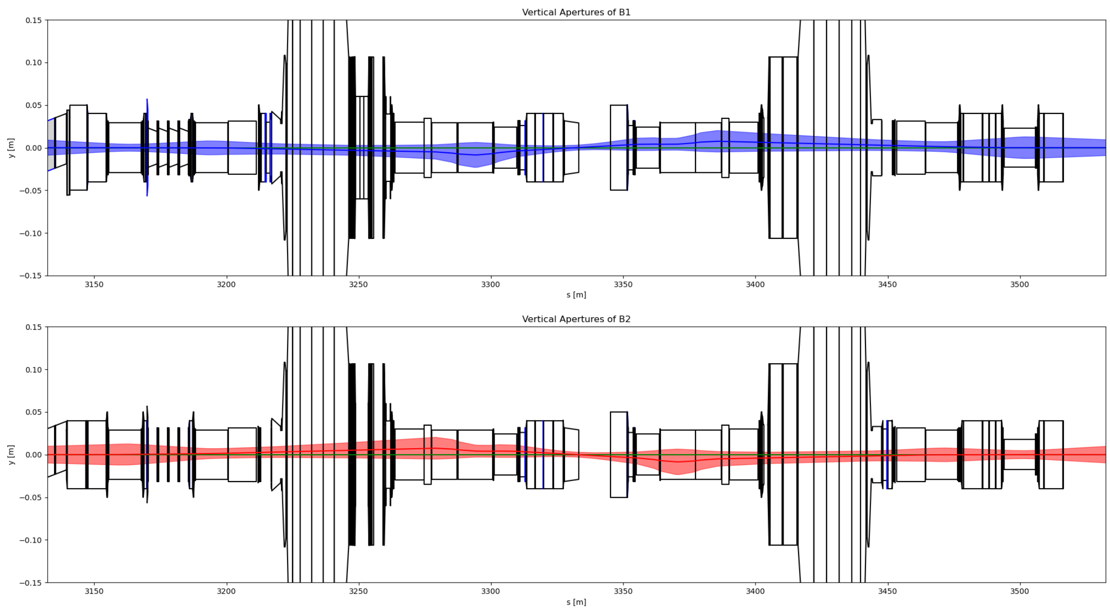

Figure 4.9: Vertical apertures and layout around IP2, with Beams and beam sizes at 10.6 σ at injection energy

4.4 Outcomes

Despite the fact that the library is at a proof of principle level, it has helped the engineering identify and fix many issues, most of them unidentified before. Some examples are shown below. It is important to note that when two elements are overlapping, then the element on the left is plotted in blue instead of black. In the first issue, Figure 4.10, the overlapping elements were moved or removed to solve the issue, Figure 4.11, the issue is available in [2]. The situation was similar for the second issue, in Figures 4.12 and 4.13, where there was some old equipment still installed [1]. For the third and fourth cases, the elements were misplaced, [32].

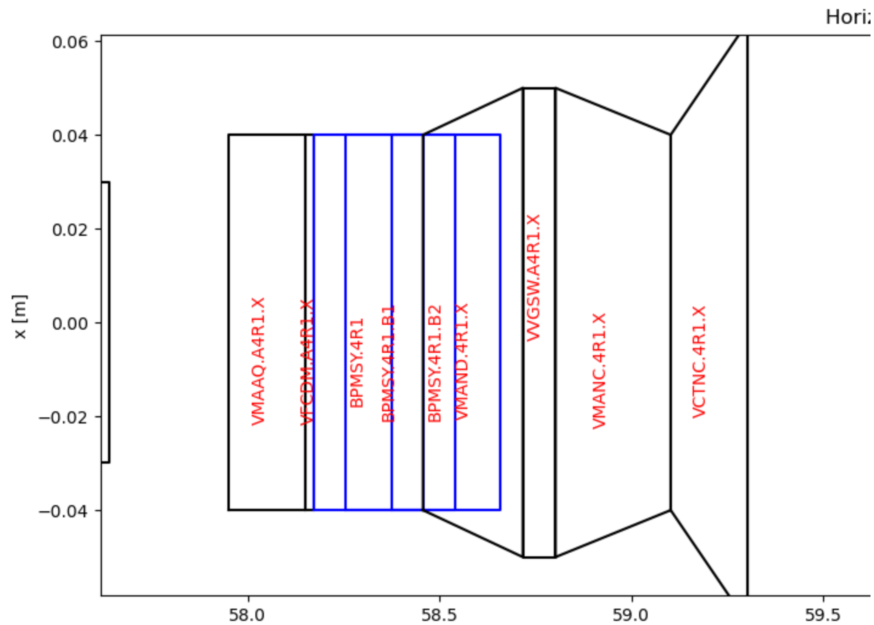

Figure 4.10: Example of overlapping elements issue

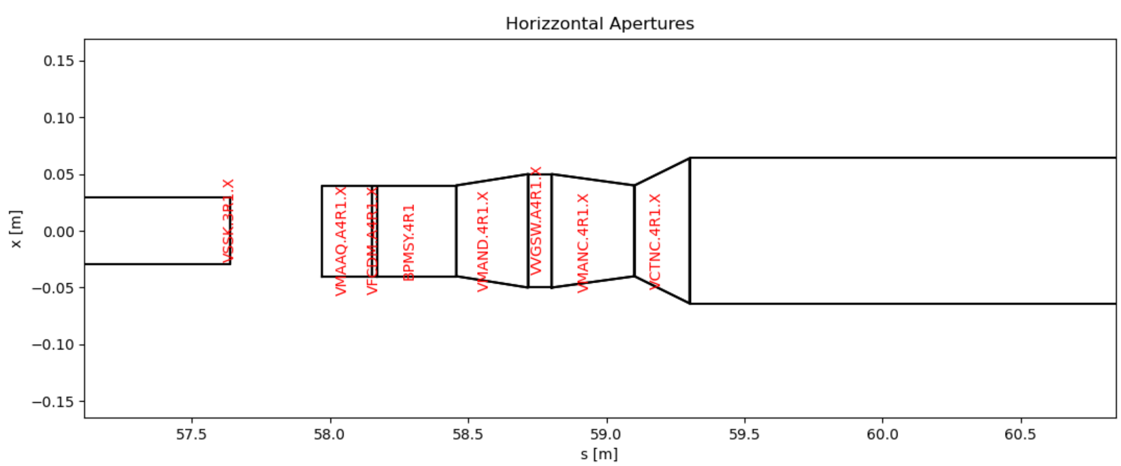

Figure 4.11: Solution to the overlapping elements [2]

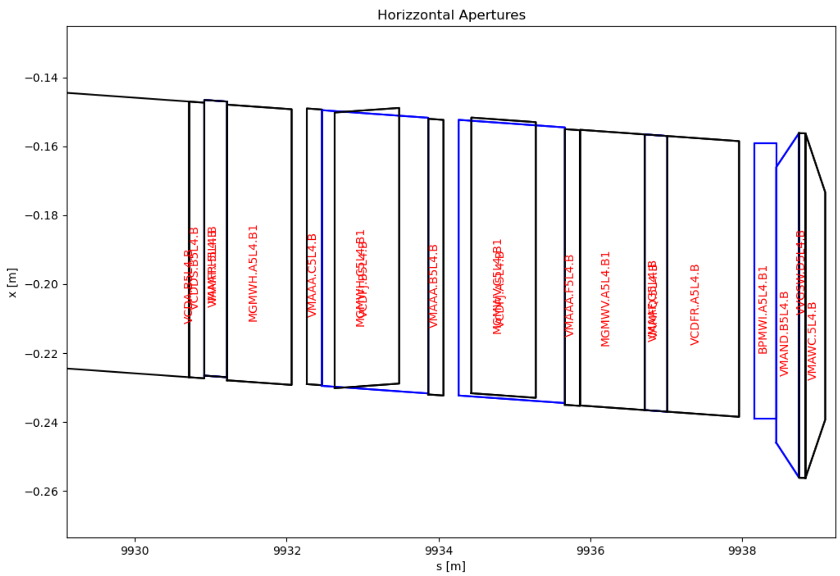

Figure 4.12: Overlapping elements

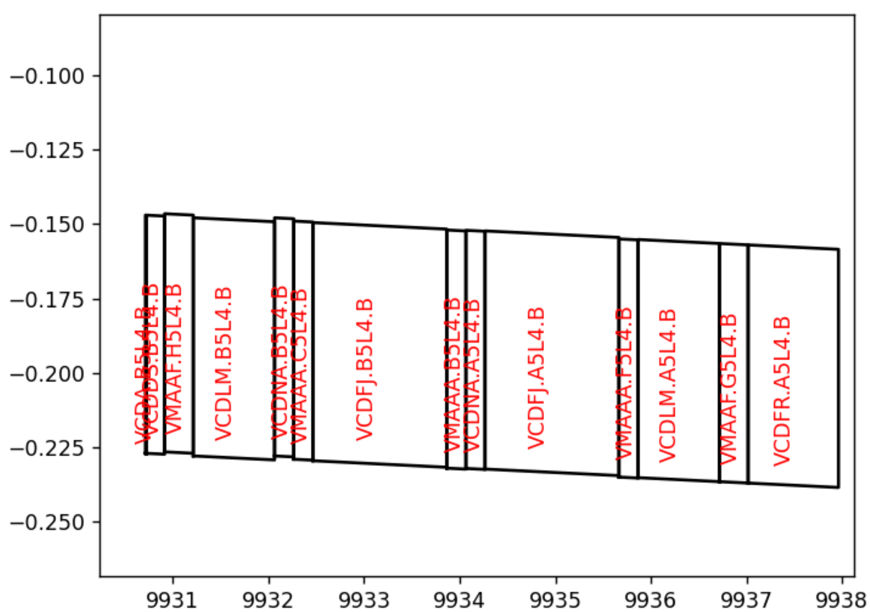

Figure 4.13: Solution to the overlapping elements [2]

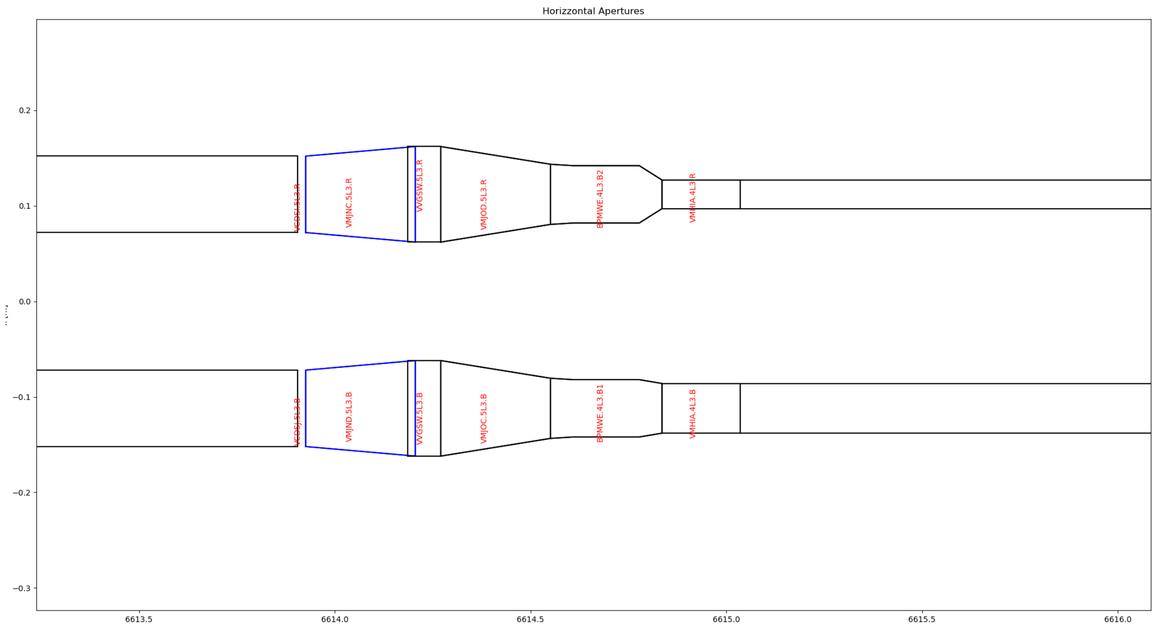

Figure 4.14: Example of misplaced elemnt

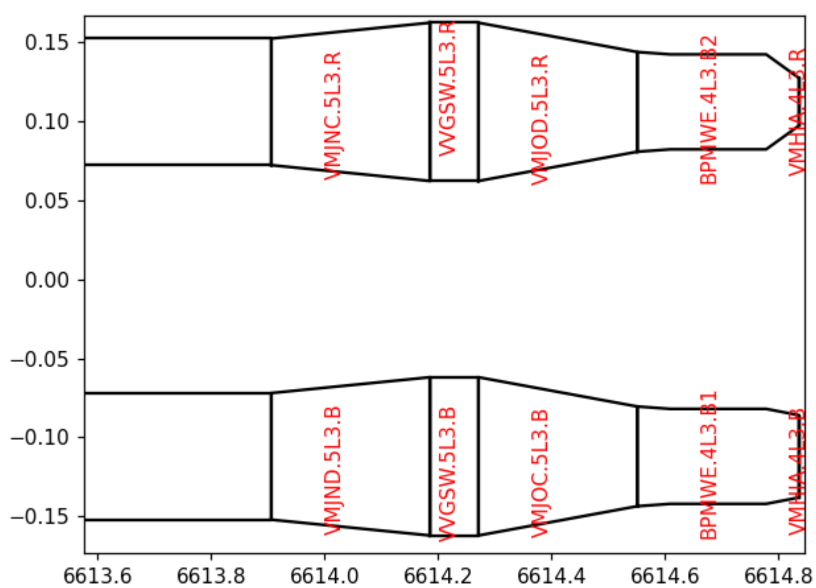

Figure 4.15: Element correctly placed

Chapter 5
Conclusion

As the case examples of TDIS, TCLIA, and the RF cavities highlighted, it is crucial to have a precise and correctly placed and aligned aperture along the machine. An accurate aperture and layout model can facilitate designing the machine optics and predict the performance of the machine well before commissioning, saving valuable time. Having such a model can also predict the losses around the machine more accurately, and help to set important parameters for the collimators around the machine. The proposed library, although it is at proof of principle level, has received positive feedback when first presented in the E2A meeting 15, [23], when there was also a small tutorial on SWAN. Since then, it has been useful to work on LHC aperture, facilitating the detection and correction of errors, in real-time, as the changes made are immediately visible. In LDB, the results of a change, are visible only in the next day. Additionally, the library provides a lot of flexibility in terms of usage, as a lot of emphasis was given to making a tool straightforward to use, even to users that are not familiar to Python. Overall, the PyLayout library can be a valuable tool for both accelerator physicists and engineering teams, providing detailed aperture analysis for the LHC that will contribute to the ensemble of the tools used to optimize the machine's operational scenarios and design aspects.

Directions of Future Work

At the time being, a module to provide survey data in LDB is being implemented, to replace the need of using the survey data from MAD-X. Given that, we can use the data directly from LDB to place the elements in global coordinates. Afterward, the way to generate the aperture shapes can be changed to use directly the computed data from LDB, as at the moment we are still using transformation tables and the data are dependent on the views extracted from the database. Since the library was useful to EN-ACE and TE-VSC teams, it can be developed further by improving many aspects such as the plotting style, labeling, and interaction of the plots. As a step further, the library could also support a 3D viewer, as some of the code towards this goal has already been implemented.

Bibliography

[1] https://its.cern.ch/jira/projects/BVACLDB/issues/BVACLDB-299?filter=doneissues.

[2] https://its.cern.ch/jira/browse/BVACLDB-292.

[3] Oliver Aberle. HCTCLIA186 type in LDB. Layout Database ID: 357005. https://layout-alt.cern.ch/classification?id=2078185&tab=APERTURE_ELEMENT_TYPE&parentId=833507.

[4] Aperture shape for TCLIA. https://acc-models.web.cern.ch/svg-path-editor/#P=M0-29.5-54-29.5-54-28A90_35_0_00-54_28L-54_29.5_0_29.5_0_35A90_35_0_000-35Z.

[5] D. Carbajo Perez at al. TDIS P8 - Alignment in the tunnel after installation. EDMS 2494157. https://edms.cern.ch/document/2494157/1.0.

[6] J. BARRAL. ACS INTERNAL GEOMETRY. EDMS 624745 v.AA — LHCACSGA0027 v.AA. https://edms.cern.ch/document/624745/AA.

[7] C. Bracco. TCLIA.R2 alignment and cross-talk with Beam 2. Presentation. https://indico.cern.ch/event/1172499/.

[8] R. De Maria C. Bracco. NCR - TCLIA misalignment after installation. EDMS 2891131 v.1 LHC-TCLIA-QN-0001 v.1. https://edms.cern.ch/document/2891131/1.

[9] CYRIL CADIOU. TDIS alignment procedure. EDMS 2433171. https://edms.cern.ch/document/2433171/1.0.

[10] M. Gonzalez de la Aleja. WP14: TDIS INTEGRATION STUDY. EDMS 1904983. https://edms.cern.ch/document/1904983/2.

[11] M. Gonzalez de la Aleja at al. TDIS P2 - Alignment in the tunnel after installation. EDMS 2407349. https://edms.cern.ch/document/2407349/1.0.

[12] Laurent Deniau (editor) Hans Grote Ghislain Roy Frank Schmidt. The mad-x program - user's reference manual. https://mad.web.cern.ch/mad/webguide/manual.html.

[13] Bernhard Holzer. Transverse Beam Dynamics Lectures during JUAS. https://indico.cern.ch/event/1210739/timetable/?view=standard.

[14] J. Jowett. ALICE ZDC aperture requirements, WP14 Meeting – TCLIA. EDMS 1830131. https://edms.cern.ch/file/1830131/1/WP14_28Feb2017_Jowett.pptx.

[15] Alexandre Lasheen. Longitudinal Beam Dynamics Lectures during JUAS. https://indico.cern.ch/event/1210739/timetable/?view=standard.

[16] P. MAESEN. GENERAL ASSEMBLY - DRAWING 1. EDMS 160002 v.AB — LHCACSGA0003 v.AB. https://edms.cern.ch/document/160002/AB.

[17] P. MAESEN. GENERAL ASSEMBLY - DRAWING 2. EDMS 160133 v.AB — LHCACSGA0004 v.AB. https://edms.cern.ch/document/160133/AB.

[18] C. Bracco A. Lechner D. C. Perez A. Perillo Marcone. TDIS - Functional Specification. EDMS 1865250 v.2.0. https://edms.cern.ch/document/1865250/2.0.

[19] R. De Maria. TCLIA aperture. Presentation. https://indico.cern.ch/event/1172499/.

[20] Syrmatenia Lampaki Riccardo De Maria. ACSCA aperture and optics studies. EDMS 2996195. https://edms.cern.ch/document/2996195/0.1.

[21] Syrmatenia Lampaki Riccardo De Maria. TCLIA.4R2 aperture and optics studies. EDMS 2996205. https://edms.cern.ch/document/2996205/0.1.

[22] Syrmatenia Lampaki Riccardo De Maria. TDIS Aperture analysis for layout database and optics studies. EDMS 2927062. https://edms.cern.ch/document/2927062/0.1.

[23] E2A meeting 15 Aperture data management. Thursday Jan 25, 2024. https://indico.cern.ch/event/1358191/.

[24] Joao Oliveira. Private communication 2024.

[25] Miguel CHASTRE RODRIGUES R. DE MARIA Eric PAGE. Aperture Profiles in the Layout Database. EDMS 2405052. https://edms.cern.ch/document/2405052/1.0.

[26] R. PERRET. TCLIA - TCTVB COLLIMATOR - GENERAL ASSEMBLY. EDMS 813967 v.0. https://edms.cern.ch/document/813967/0.

[27] R. PERRET. TCLIA AND TCTVB COLLIMATOR - INTER ASSEMBLY. EDMS 831459 v.AA. https://edms.cern.ch/document/831459/AA.

[28] R. PERRET. TCLIA COLLIMATOR - TANK ASSEMBLY. EDMS 813966 v.AB. https://edms.cern.ch/document/813966/AB.

[29] A. Abramov D. Mirarchi S. Redaelli. Loss maps and status of collimation validation, 35th ABP-NDC section meeting. Presentation. https://indico.cern.ch/event/1162318/.

[30] O. Aberle V. Baglin C. Bracco P. Santos Diaz J. Jowett I. Lamas Garcia W. Riegler. TCLIA.4R2.B1 modifications. EDMS 1936597 v.1.0 LHC-TC-EC-0011 v.1.0. https://edms.cern.ch/document/1936597/1.0.

[31] Michaela Schaumann. Particle Accelerators and Beam Dynamics Lectures on the Summer Student Programme 2022. https://indico.cern.ch/event/1132546/.

[32] https://its.cern.ch/jira/projects/BVACLDB/issues/BVACLDB-300?filter=doneissues.

[33] Svgpatheditor, 300 mm circlular aperture. https://acc-models.web.cern.ch/svg-path-editor/#P=M_150,_0_a_150,150_0_1,0_-300,0_a_150,150_0_1,0_300,0.

[34] Svgpatheditor, 686.8 mm circlular aperture. https://acc-models.web.cern.ch/svg-path-editor/#P=M_343.4,_0_a_343.4,343.4_0_1,0_-686.8,0_a_343.4,343.4_0_1,0_686.8,0.

[35] SvgPathEditor, aperture shape for the third module. https://acc-models.web.cern.ch/svg-path-editor/#P=M_0_4_h_78.4_a_60_60_0_0_1_0_120_h_-78.4_h_-4_v_-5_h_-62_v_5_h_-4.5_v_-120_h_4.5_v_5_h_62_v_-5_z.

[36] SvgPathEditor, aperture shape for transitions 1 and 2. https://acc-models.web.cern.ch/svg-path-editor/#P=M_68_60.2_a_60.2_60.2_90_0_0_0_-120.4_h_-68_h_-61.5_a_17_17_90_0_0_-17_17_v_86.4_a_17_17_90_0_0_17_17_h_61.5_z.

[37] E. Urrutia. TDIS 1st MODULE ASSEMBLY TDIS INJECTION DUMP. EDMS 1700650. https://edms.cern.ch/document/1700650/AB.

[38] E. Urrutia. TDIS INJECTION DUMP - TDIS TRANSITION 1 - CHAMBER TUBE. EDMS 1763058. https://edms.cern.ch/document/1763058/AB.

[39] E. Urrutia. TDIS INJECTION DUMP - TDIS TRANSITION 2 - CHAMBER. EDMS 1840135. https://edms.cern.ch/document/1840135/AA.

[40] E. Urrutia. TDIS R8 ASSEMBLY TDIS INJECTION DUMP - LHCTDIS_0254 v.0. EDMS 2133886 v.0. https://edms.cern.ch/document/2133886/0.

Appendix A
Acronyms and Abbreviations

LDB Layout Database

TDIS Beam Absorber for Injection Segmented

TDI Beam Absorber for Injection

TDISA Beam Absorber for Injection Graphite Block

TDISB Beam Absorber for Injection Graphite Block

TDISC Beam Absorber for Injection Copper/Titanium block

ECR Engineering Change Request

MAD-X Methodical Accelerator Design, X stands for the current version

YETS Year-End Technical Stop

EDMS Engineering & Equipment Data Management Service

SVG Scalable Vector Graphics

ZDC Zero Degree Calorimeter

RF Radio Frequency

B1 Beam 1

B2 Beam 1

ABP Accelerator and Beam Physics

EN - ACE Engineering Department - Accelerator Coordination & Engineering group

TCLIA Collimator for Injection Protection at D1

SWAN Service for Web based Analysis

IP Interaction Point

DCUM Distance Cumulated

SRF Superconducting RF Cavities